# 國 立 交 通 大 學

## 機 械 工 程 學 系
## 碩 士 論 文

以直接模擬蒙地卡羅法模擬多蒸鍍源之物理氣相沉

積過程

DSMC Simulation of the Physical Vapor Deposition Process

with Multiple Sources

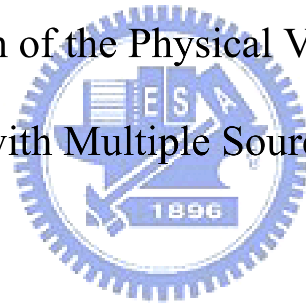

研究生：陳育進
指導教授：吳宗信 博士

中 華 民 國 九 十 五 年 七 月

以直接模擬蒙地卡羅法模擬多蒸鍍源之物理氣相沉積過程

# DSMC Simulation of the Physical Vapor Deposition Process with Multiple Sources

研 究 生：陳育進 Student: Yu-Jin Chen
指導教授：吳宗信 博士 Advisor: Dr. Jong-Shinn Wu

國立交通大學
機械工程學系
碩 士 論 文

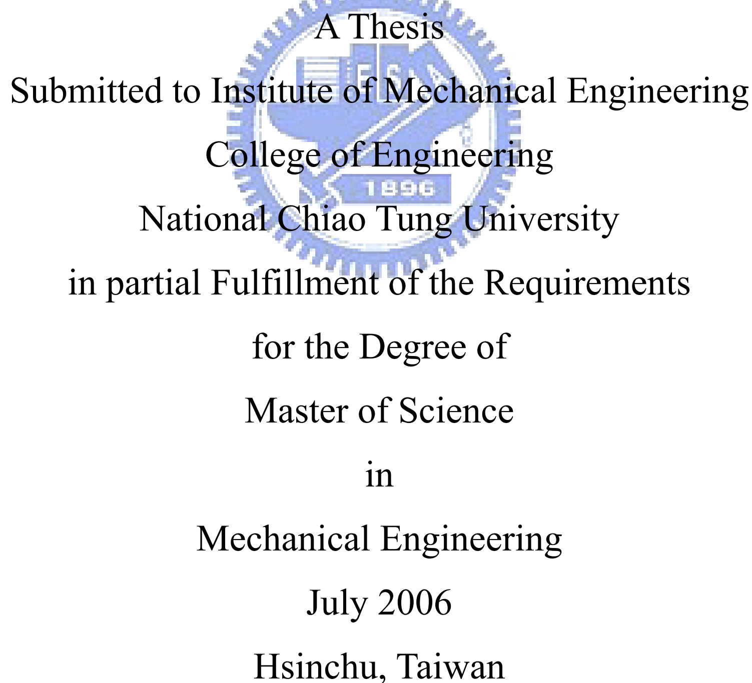

A Thesis
Submitted to Institute of Mechanical Engineering
College of Engineering
National Chiao Tung University
in partial Fulfillment of the Requirements
for the Degree of
Master of Science
in
Mechanical Engineering
July 2006
Hsinchu, Taiwan

中華民國九十五年七月

# 致謝


碩士班的生活將告一個段落，隨即開始的是另一個階段的人生，在交大兩年的求知路程，特別感謝指導教授吳宗信老師的諄諄教誨，與老師的知識交流實令我感到獲益匪淺，讓我能順利的踏入研究的領域並且不斷地成長。另外特別感謝連又永學長，你不吝於付出時間與心力來教導我於研究中所遭遇的問題，並時時督促著我前進，其認真的臉龐將永遠刻畫在我心頭，感謝你。還有 MuST 實驗室的每一位成員，許佑霖、邵雲龍、許國賢、李允民、周欣芸、李富利、洪捷粲、許哲維、鄭凱文學長姊，梁偉豪、胡孟樺、陳百彥同學，及洪維呈、盧志偉、謝昇汎、陳又寧、王柏勝、林宗漢學弟，與你們相處的時光將是我最美好的回憶。最後感謝我的父母從小到大的扶養及栽培，及女友珍蘭的陪伴與鼓勵，和我分享生活中的喜怒哀樂。

兩年的時光很快地過去了，心中帶有些喜悅卻有些不捨，在交大求學的這段日子裡，充滿了許多的美好及深刻回憶，展望著未來期待自己能發揮所學貢獻微薄的心力於社會上。希望珍惜這個緣份與實驗室的每位在將來能夠互相聯繫，並祝福你我皆有個光明的未來及美滿的生活。

# 以直接模擬蒙地卡羅法模擬多蒸鍍源之物理氣相沉積過程

學生：陳育進　　　　　　　　　　　　　　　　　　　　　　指導教授：吳宗信 博士

國立交通大學機械工程學系

## 摘要

在過去的數十年，電子束物理氣相沉積是一門被廣為發展的技術。應用此項技術的領域非常廣泛，特別是在半導體及航太工業，對鍍膜的應用實有著相當的貢獻。在這篇論文裡，首先介紹物理氣相沉積的基本理論，隨後敘述著合金沉積的概念，接著有幾個重要的課題值得我們去研究－基板上沉積的厚度及合金成分之均勻性。因此我們利用直接模擬蒙地卡羅法來模擬此項研究。為了了解流場中的傳輸現象，我們首先模擬一個簡單的案例，腔體內只有一個蒸鍍源，比較有考慮腔體內的背壓效應及沒有考慮腔體內的背壓效應的影響下，可以很明顯的看出腔體內的密度、溫度及速度變化之差異性。接著我們取金屬鈦、鋁、釩來做為蒸鍍物，利用多蒸鍍源之物理氣相沉積系統來沉積一個應用性極廣的鈦合金 Ti6Al4V。藉著改變參數包括基板的高度、背壓及蒸鍍源之間的距離，基板上的沉積結果將告訴我們應如何調整才能得到令人可接受的厚度及合金成份之均勻性。

**DSMC Simulation of the Physical Vapor Deposition Process with Multiple Sources**

Student: Yu-Jin Chen Advisor: Dr. Jong-Shinn Wu

Institute of Mechanical Engineering
National Chiao Tung University

# Abstract

The technology of electron beam physical vapor deposition (EBPVD) has been highly developed in the past decades. It is widely used in many fields, especially in the semiconductor and aerospace industry. Its application really contributes to coating. In this study, the basic theory about electron beam physical vapor deposition will be introduced. The concepts about the deposition of alloy are then described subsequently. There are some important subjects we need to investigate, that is, the uniformity of deposited thickness and composition on the substrate. As a result, we use Direct Simulation Monte Carlo (DSMC) method to model this simulation conditions. In order to understand the transport phenomena, we simulate a simple case first, one source in the chamber. It is obvious to see the differences of variation of density, temperature, and velocity with and without considering background gas effect. Then we take metals of titanium, aluminum, vanadium as evaporant to coat with a widely applied titanium alloy Ti6Al4V using multiple sources EBPVD system. By changing parameters including altitude of the substrate, background pressure and distance between the sources, the deposited results on the substrate will show how we should adjust to obtain acceptable uniformity of

thickness and composition.

# Table of Contents


**致謝** .................................................. **I**

**摘要** .................................................. **II**

**Abstract** .................................................. **III**

**Table of Contents** .................................................. **V**

**List of Figures** .................................................. **VIII**

**List of Tables** .................................................. **XI**



**List of Tables** .................................................. **XI**



**Nomenclature** .................................................. **XII**

**Chapter 1 Introduction** .................................................. **1**

1-1 Motivation .................................................. 1

1-2 Modeling of Electron Beam Physical Vapor Deposition Process .................................................. 2

1-2-1 Overview .................................................. 2

1-2-2 Vapor propagation .................................................. 5

1-2-3 Alloy Deposition .................................................. 7

1-3 Literature Survey .................................................. 9

1-4 Specific Objectives of the Thesis .................................................. 12

**Chapter 2 Numerical Method** .................................................. **13**

2-1 DSMC Method .................................................. 13

2-2 Parallel DSMC Method .................................................. 14

2-2-1 Unstructured Tetrahedral Mesh .................................................. 16

2-2-2 Collision Cross-Section Data .................................................. 17

2-2-3 Pressure Boundary Treatment ........ 18

2-2-4 Unstructured Adaptive Mesh with Variable Time-Step Scheme ........ 19

2-2-5 Parallel with Dynamic Domain Decomposition........ 24

2-2-6 Conservative Weighting Scheme........ 24

2-2-7 Molecular Chemical Reaction ........ 27

**Chapter 3 Results and Discussion........ 29**

3-1 Simulation Conditions of one source........ 29

3-1-1 Verification of Flux Distribution ........ 30

3-1-2 Variations of Inflow Field........ 31

3-1-3 Comparison of Simulations with and without Background Gas ........ 32

3-2 Simulation Conditions of Multiple Sources ........ 33

3-2-1 Uniformity of Composition........ 34

3-2-2 Uniformity of Thickness ........ 35

3-2-3 Growth Rate ........ 36

3-3 Uniformity Discussion of Different Parameters ........ 36

3-3-1 Altitude of the Substrate ........ 37

3-3-2 Background Pressure........ 37

3-3-3 Distance between the Sources ........ 38

**Chapter 4 Conclusions ........ 39**

4-1 Summary........ 39

4-2 Recommendation ........ 40

**References ........ 41**

**Appendix A ........ 46**

**Appendix B** ............................................................................................................. 48

**Tables**........................................................................................................................ 49

**Figures**....................................................................................................................... 56

# List of Figures

Fig. 1.1 Principle of electron beam evaporation. [Schiller, *et al*., 1982] .......................... 56

Fig. 2.1 Conventional DSMC flow chart. ........................................................................ 57

Fig. 2.2 Simplified flow chart of the parallel DSMC method for np processors. ............. 58

Fig. 2.3 Schematic diagram of the proposed cell numbering scheme. ............................. 59

Fig. 2.4 The additional schemes in the parallel DSMC code. .......................................... 60

Fig. 2.5 Sketch of the concept of variable time step scheme. .......................................... 61

Fig. 2.6 The flowchart of the parallel DSMC method with dynamic domain decomposition method. ........................................................................ 62

Fig. 2.7 Schematic diagram of CWS for non-reactive flow. ............................................ 63

Fig.2.8 The flow chart of chemical reaction in the PDSC. .............................................. 64

Fig. 3.1 Verification of inflow condition: quarter half sphere for simulation region. ....... 65

Fig. 3.2 Normalized vapor flux distributions from titanium disk sources at 2050 K with five different diameters, and $\cos(\theta)$ for reference. ........................................... 66

Fig. 3.3 Inflow condition simulation: density distribution. ............................................. 67

Fig. 3.4 Inflow condition simulation: temperature distribution. ...................................... 68

Fig. 3.5 Inflow condition simulation: z-directional velocity distribution. ........................ 69

Fig. 3.6 Inflow condition simulation: velocity vector. ..................................................... 70

Fig. 3.7 Three view drawing of the chamber. .................................................................. 71

Fig. 3.8 Inflow condition of quart chamber that contains one source on the bottom: (a) density; (b) temperature; (c) z-directional velocity; (d) velocity vector. ............ 72

Fig. 3.9 Comparisons of inflow condition with vacuum(left) and background pressur

$5\times10^{-5}$ torr (right): (a) density; (b) temperature; (c) z-directional velocity. ...... 73

Fig. 3.10 Comparisons of inflow condition with different background pressure $2.5\times10^{-5}$ torr(left), $5\times10^{-5}$ torr(middle), $7.5\times10^{-5}$ torr(right): (a) density; (b) temperature; (c) z-directional velocity. ............................................................ 74

Fig. 3.11 Comparison of the number deposited particle with (a) vacuum (b) background pressure $7.5\times10^{-5}$ torr. ......................................................................... 75

Fig. 3.12 The specific cell labeled to sample the distribution of energy and incident angle. ................................................................................................................ 76

Fig. 3.13 Comparison of energy distribution with vacuum (solid line) and background gas $3.11\times10^{-5}$ torr (dash line): (a) face 1; (b) face 2; (c) face 3; (d) face 4; (e) face 5; (f) face 6; (g) face 7; (h) face 8. ...................................................................... 77

Fig. 3.14 Comparison of incident angle distribution with vacuum (solid line) and background gas $3.11\times10^{-5}$ torr (dash line): (a) face 1; (b) face 2; (c) face 3; (d) face 4; (e) face 5; (f) face 6; (g) face 7; (h) face 8. ........................................... 78

Fig. 3.15 The relative position of three sources and substrate in the simulation domain. 79

Fig. 3.16 The position of evaporated atoms at a specific steady time step (a) titanium; (b) aluminum; (c) vanadium; (d) together with titanium, aluminum and vanadium. 80

Fig. 3.17 Vapor pressure and Langmuir evaporation rates for titanium, aluminum and vanadium over the range 1600-2200℃. Small circles lie at melting points, and gray vanadium curves are extrapolations of solid data.[Powell, 1997] .............. 81

Fig. 3.18 The distributions of composition of alloy on the substrate (a) titanium; (b) aluminum; (c) vanadium. ..................................................................... 82

Fig. 3.19 The distribution of error percentage of individual evaporated atom on the

substrate (a) titanium; (b) aluminum; (c) vanadium. ........................................ 83

Fig. 3.20 The distribution of thickness on the substrate. ................................................ 84

Fig. 3.21 The distribution of the growth rate at (a) time step 5000~15000; (b) time step 15000~25000; (c) time step 25000~35000. ..................................................... 85

Fig. 3.22 The comparisons of composition and thickness. The rows of left, middle and right represent three different altitude of the substrate: 10cm, 27.5cm and 40cm. The columns represent (a) titanium; (b) aluminum; (c) vanadium; (d) thickness. ............................................................................................................................ 86

Fig. 3.23 The comparisons of composition and thickness. The rows of left, middle and right represent three different background pressure: $5\times10^{-5}$, $5\times10^{-6}$ torr and vacuum. The columns represent (a) titanium; (b) aluminum; (c) vanadium; (d) thickness.......................................................................................................... 87

Fig. 3.24 The comparisons of composition and thickness. The rows of left, middle and right represent three different distances between sources: 1.732, 4.330 and 6.928cm. The columns represent (a) titanium; (b) aluminum; (c) vanadium; (d) thickness.......................................................................................................... 88

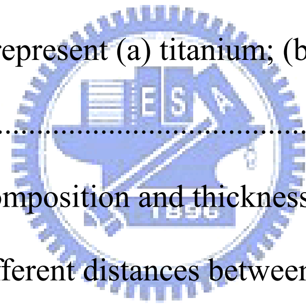

# List of Tables

Table I. The properties of Ti, Al, V. ........ 49

Table II. The composition of Ti6Al4V ........ 50

Table III. Typical physical properties for Ti6Al4V. ........ 51

Table IV. Typical mechanical properties for Ti6Al4V. ........ 52

Table V. The relevant values of Ti6Al4V compared with different altitude of the substrate: (a) 10 cm ; (b) 27.5 cm ; (c) 40 cm. ........ 53

Table VI. The relevant values of Ti6Al4V compared with different pressure in the chamber: (a) $5\times10^{-5}$ torr ; (b) $5\times10^{-6}$ torr ; (c) vacuum. ........ 54

Table VII. The relevant values of Ti6Al4V compared with different distances between the sources: (a) 1.732 cm ; (b) 4.330 cm ; (c) 6.928 cm. ........ 55

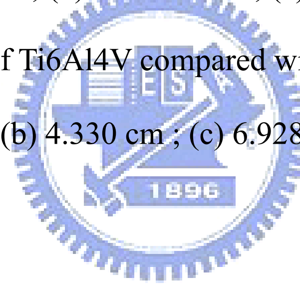

# Nomenclature

| | |
|---|---|
| $A$ | area of the cell |
| $A_{cls}$ | bottom area of the crystal lattice structure |
| $a$ | the distance between adjacent lattice points in the basal plane |
| $c$ | height of the crystal lattice structure |
| $d$ | diameter of the source |
| $d_S$ | the film thickness which is apart $d_{S0}$ from $r_S$ on the substrate |
| $d_{S0}$ | film thickness for $\alpha = 0$ on the substrate |
| $E$ | energy |
| $h_v$ | the distance of the substrate plane from the source |
| $J$ | specific evaporation rate |
| $Kn$ | Knudsen number |
| $k$ | Boltzmann constant, $k = 1.3807 \times 10^{-23}\ joule / K$ |
| $L$ | characteristic dimension |
| $l$ | the distance between the sources |
| $M$ | molecular mass of the evaporating species |
| $N_p$ | number of simulated molecules of $p^{\text{th}}$ cell |
| $N_{tot}$ | total deposited particles in a unit cell |
| $n$ | number density |
| $n_{cls}$ | lattice points per crystal lattice structure |
| $P$ | momentum |
| $p_v$ | vapor pressure of the evaporant |
| $R_g$ | ideal gas constant |
| $r_S$ | the distance between the normal to the source center and the substrate any point under consideration |
| $T$ | absolute temperature of the source |

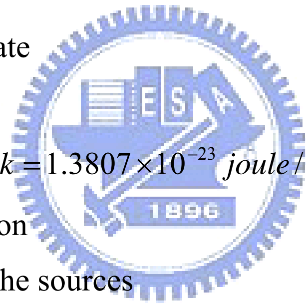

$u$ molecular velocity

$V$ volume of the computational cell

$W_p$ particle weight

$\alpha$ the angle from the normal to the vapor emitting surface

$\lambda$ mean free path

$\lambda_0$ equivalent mean free path

$\sigma$ collision diameter

$\Phi_0$ vapor stream for $\alpha = 0$

$\Phi(\alpha)$ vapor flux distribution

$\Phi$'s conserved flux quantity

$\Delta t_i$ time step in cell $i$

$\Delta x$ $V^{1/3}$,characteristic length of the cell

# Chapter 1 Introduction

## 1-1 Motivation

Evaporation in vacuum is a significant process for the production of thin films. Through knowledge of physical and applicative features of the films and the results of considerable technological efforts in the field of evaporation techniques have increased industrial application of these techniques in many fields. The advent of electron beam evaporation in vacuum coating has therefore exerted a strong impetus on this development.

Electron beam evaporation is used to form coatings of a wide variety of materials, from metals to ceramics to semiconductors, with many different applications. Metal lines in microelectronic devices are most often produced either by sputtering or electron beam evaporation [Wolf and Rauber, 1986]; ceramic thermal barrier coatings are evaporated onto turbine blades [DeMasi-Marcin and Gupta, 1994]; various protective coatings are evaporated onto steel strip [Bakish, 1995]; and a new class of titanium-matrix composites is being made by evaporating titanium alloys onto fibers and subsequently consolidating them into a dense composite with high fiber volume fraction [Storer, 1993; Storer, 1996].

For different applications, the desired coating thickness distribution varies as well. In many cases, a uniform thickness distribution is desired, such as alloy; in others where yield is more important, such as metal-matrix composites, a narrow plume is desired. This area of the research is therefore devoted to analysis of the vapor flux distribution as a function of source temperature distribution, in order to design beam patterns which give rise to desired coating thickness distributions.

In previous documents and theses, there are not so many reports discussed the

three-dimensional computation model about flow simulator in the field of electron beam physical vapor deposition (EBPVD). In order to understand the phenomena of evaporation kinetic transport, I take advantage of Direct Simulation Monte Carlo method [Bird, 1994] to simulate the production of alloy in the chamber of multiple sources. To find what process parameters in constant evaporant surface temperature that substrate will achieve film thickness uniformity and composition we desire.

## 1-2 Modeling of Electron Beam Physical Vapor Deposition Process

### 1-2-1 Overview

Basically, physical vapor deposition is a vacuum coating process in which a directed vapor stream propagates from the evaporator to the substrate. Since generation and guidance of the beam must also take place in a vacuum, evaporation in this design should be happened in vacuum environment. As a result, system requires highly vacuum equipment. Fig. 1.1 shows the principle of electron beam evaporation. A plant for electron beam evaporation consists of a work chamber with a vacuum pumping system, a crucible for the evaporant, an electron gun, and a substrate with its fixtures and heating appliances. In contrast to conventional heating modes, the evaporant is heated by a beam that impinges directly onto its surface; the greatest portion of the kinetic energy in the beam is converted into heat. The surface is therefore brought to such a high temperature that it becomes the source of a vapor stream. After a series of collisions between vapor particles, the particles approach substrate quickly. The substrate to be coated is arranged in this vapor stream and part of the vapor condenses on it in the form of a thin film. Here, one design is important; we must focus on the position of electron gun in the chamber.

Because of the simultaneous phenomena of evaporation and deposition, collisions between evaporated atoms are isotropic. In order to provide steady electron beam and prevent from damaging due to deposition, a **270**° gun is often used. It usually locates on the outside of chamber, depending on magnet system to change electron beam direction and impinge on the evaporant. The concept above can be understood by right hand rule. An electron in motion in a magnetic field experiences an electromagnetic force perpendicular to its direction and to the magnetic field.

The electron beam physical vapor deposition process is composed of three sections that we need to study. First, inclusion dissolution and flotation behavior in the melting/refining hearth, heat transfer, fluid flow and melt interface shape in the hearth. Such models are reported elsewhere in the literature [Bellot, *et al.*, 1993; Bellot, *et al.*, 1998]. Second, evaporation kinetics in a periodically-heated surface. It is shown that beam scan frequency has a significant effect on evaporation rate from a molten pool, which may be used for control of composition in electron beam melting, and in conjunction with power for somewhat independent control of evaporation rate and source temperature in electron beam evaporation. The third, rarefied gas dynamics in electron beam evaporation, and an evaluation of source geometry designs for exercising some control over coating thickness distribution on the substrate. The vapor interactions above the melt can have a tremendous effect on the vapor flux distribution, and also on the recondensation of evaporated atoms back into the melt due to collisions in the vapor phase. This recondensation is discussed as a possible source of error in the evaporation rate calculations. It is reported [Powell, 1997] that the recondensation fraction is a function of the ratio of source diameter to equivalent mean free path $d/\lambda_0$, and can

climb as high as around 10%, even without background gas present.

For vaporization of a substance in a high vacuum, the specific evaporation rate $J$, the amount evaporated per unit time per unit area, according to Langmuir's equation:

$$J = \frac{p_v}{\sqrt{2\pi M R_g T}} \tag{1.1}$$

where $R_g$ is the ideal gas constant, $T$ the absolute temperature, $M$ the molecular mass of the evaporating species, and $p_v$ its vapor pressure. The vapor pressure of a pure species $\overline{p_v}$ can in turn be estimated using the Clausius-Clapeyron equation

$$\log \overline{p_v} = -\frac{A}{T} + B + C\log T + 10^{-3} DT \tag{1.2}$$

where pressure is given in torr. $A$, $B$, $C$ and $D$ are constants associated with the evaporating species and listed in Ref. [Brandes, 1983].

The strongly nonlinear nature of Eq. 1.1 and 1.2 make evaporation rate extremely sensitive to temperature fluctuations. These fluctuations are governed by the beam power, spot size, frequency, and ability of the molten material to dissipate heat from the surface by conduction, convection, radiation and evaporation. Heating is by electron impact, and the dominant flow drivers are Marangoni shear and buoyancy. Evaporation can be said to fall into four regimes, presented here in terms of scan frequency for a given pattern geometry:

1. At very high frequencies (> 400 Hz), the dwell time will be very short (< 30 μsec) and the temperature fluctuations relatively small (~250℃), so evaporation near the beam spot will not be a significant fraction of total evaporation and power can be considered uniformly distributed over the scan pattern.

2. At high frequencies (60-400 Hz), the beam will generate a hot spot temperature high enough to affect evaporation rates (250-650℃ above surroundings), though this will not cause significant transient fluid flow. The low Prandtl number of metals leads to longer time scales for fluid flow than heat transfer, making possible significant transient heating without significant transient flow at these frequencies.
3. At moderate frequencies (20-60 Hz), transient flow generated by Marangoni shear is sufficiently strong to significantly modify temperature fluctuations and affect evaporation rates. The onset of significant flow can be estimated using the Peclet number as described in appendix A.
4. At low frequencies (< 20 Hz), various other phenomena may affect surface temperature, such as turbulent fluid flow, ionized metal vapor interfering with the beam [Tripp and Mitchell, 1993], and depressions in the melt surface generated by large vapor pressure excursions at high temperatures [Gilbaud, 1995; Tran Kong and Bird, 1978]. The transition to this regime depends on which phenomenon is dominant.

Also, there are some process parameters that will influence the evaporation rate, including beam power, pattern length, spot size, electron accelerating voltage, contamination in the evaporant, background chamber pressure, and so on.

### 1-2-2 Vapor propagation

Thin films made by electron beam physical vapor deposition play an increasingly important role in a wide variety of products and fields. However, the mechanics of vapor

transport are poorly understood, in part because rarefied gas behaviors very different form that of more familiar fluids. In particular, the stream of atoms evaporating from a surface follows the well-known cosine distribution, but in high-flux processes such as electron beam evaporation, collisions between evaporated atoms actually lead to a focusing of the vapor plume toward the surface normal, with the resulting flux distributed as $\cos^2\theta$ or even $\cos^3\theta$ [Schiller, *et al.*, 1982]. This result is completely different from the intuitive expectation that more collisions will lead to dispersing of the plume. For this reason, it has never even been considered that one could exercise any control over deposition profile in evaporation processes.

The vapor stream emerging from an evaporator is characterized by the vapor flux distribution $\Phi(\alpha)$. One approach to describing the vapor flux distribution of real small area evaporators is via a cosine function of higher order:

$$\Phi(\alpha) = \Phi_0 \cos^n \alpha \tag{1.3}$$

Where $\Phi(\alpha)$ is the vapor stream in a direction describing an angle $\alpha$ from the normal to the vapor emitting surface and $\Phi_0$ is the vapor stream for $\alpha = 0$. $n$ is greater than unity. It has been shown that the description of the vapor flux distribution of electron beam evaporators according to Eq. (1.3) is fully adequate in an angular range of up to about 30° if the evaporation rate is not too high [Schiller, *et al.*, 1982]. With growing evaporation rates, a more pronounced directional dependence is to be expected. It has been speculated that the extent of focusing should depend only on the ratio of source diameter to equivalent mean free path $d/\lambda_0$ [Powell, 1997], that is, the inverse of what might be called the local Knudsen number. The equivalent mean free path here is that given by the vapor pressure $p_v$, which is therefore

$$\lambda_0 = \frac{kT}{\sqrt{2}\pi\sigma^2 p_v} \tag{1.4}$$

giving the parameter $d / \lambda_0$ as:

$$\frac{d}{\lambda_0} = \frac{d\sqrt{2}\pi\sigma^2 p_v}{kT} \tag{1.5}$$

Now the film thickness distribution on any desired substrate arrangement will be calculated from the evaporator characteristic. One wants to know the film thickness distribution on a plane substrate or substrate arrangement parallel to the surface of a small area evaporator and finds out the relation described as:

$$\frac{d_S}{d_{S0}} = \frac{1}{[1+(\frac{r_S}{h_v})]^{(n+3)/2}} \tag{1.6}$$

Where $d_S$ is the film thickness which is apart $d_{S0}$ from $r_S$ on the substrate. $d_{S0}$ is the film thickness for $\alpha = 0$ on the substrate. $h_v$ is the distance of the substrate plane from the evaporator and $r_S$ is the distance between the normal to the evaporator center and the substrate any point under consideration. The film thickness distribution $d_S / d_{SO}$ with $n = 0$ corresponds to the case of point source evaporation.

**1-2-3 Alloy Deposition**

If alloys are to be deposited, uniform composition of the film must be obtained over the total substrate surface and film thickness. In effect, two basic principles are used for the deposition of alloys: depositions from single or multiple evaporation sources. In the case of multiple evaporation sources the constituents are separately evaporated from several crucibles, the number of which correspond to that of the alloying elements, and

jointly condensed on the substrate. Deposition from two crucibles should now be explained by using as an example a binary alloy AB, that is, an alloy made up of the constituents A and B. Separate vapor stream with evaporation rates as given by Eq. (1.1). When the crucibles are separated by a distance $l$, which is short compared to the distance $h_v$ between the substrate and the crucibles, one obtains an extended range where the vapor stream contains both alloying elements. Owing to the directional dependence of the vapor stream, however, adequate alloying constancy can be obtained only within a restricted substrate area. The influence of the geometric array on the uniform composition of the film depends on the ratio $l / h_v$.

Since the evaporation rate shows a pronounced dependence on the temperature, the accuracy of the alloy composition is limited. Thus a highly constant evaporator temperature is a necessary condition for obtaining uniform evaporation rates and represents a basic requirement for producing films of adequate alloy constancy when using co-evaporation from several crucibles.

Co-deposition can be performed with the aid of various electron beam evaporators. Another possibility is to use the beam of one gun to heat several crucibles. In this case the beam power is distributed among the individual crucibles by programmed deflection [Cron and Adams, 1969]. Beam power distribution to the crucibles take place by adjusting a defined duty cycle for the deflection currents of the beam guidance system. In this way it is possible to adjust the evaporation rates of the constituents and thus control alloy composition of the film.

Multiple-source evaporation is used in the manufacture of alloy films whenever the evaporant cannot be produced with the required composition and single-source

evaporation proves to be impossible. Mixing in the vapor phase is practical in cases where the vapor pressures of the constituents are vastly different, for example, differing by four or more orders of magnitude.

Simultaneous electron beam evaporation from two sources appeared to be a promising solution to the basic problem of controlled and reproducible deposition of alloy films. However, most alloy film deposition work seems to be still carried out by evaporation from one alloy source. Yet composition control is quite problematic and limited in this process. On the other hand, co-deposition from separate sources usually involves more complicated and expensive equipment. Difficulties are also encountered in controlling evaporation rates of the individual constituents. Employing one electron beam generated by a self-accelerated gun and oscillated in a controlled manner between two materials is a relatively simple scheme, considerably less expensive than a double-gun configuration. The dwelling time of the beam on each source determines the heat input and, therefore, the rate of evaporation of each constituent. Composition of co-deposited films can be controlled by varying the ratio of the two dwelling times.

**1-3 Literature Survey**

The development of electron beam technology into a special field of its own is closely related to the advances in vacuum engineering and electron optics. The history of this basic science has been extensively dealt with elsewhere. In 1905 Marcello von Pirani successfully carried out the first experiments on electron beam melting of refractory metals such as tantalum. But since vacuum engineering and electron optics were still in their infancy at that time there was no industrial demand for such a technique. In 1938

von Ardenne and Ruhle employed magnetic-lens systems for beam focusing to drill small bores and evaporate metals, respectively. Around 1950 Steigerwald wrote a paper on the technical possibilities of the beam as a tool for drilling and machining in the micron range. In the long run, however, the development of nucleonics and space engineering called for new technological processes for, say, welding, melting, and evaporation. In the mid-1950s this situation stimulated the use of electron beams for technological purposes. A characteristic example is Stohr's work [Stohr, 1958] on the technical development of electron beam welding. In the following years electron beam evaporation was increasingly used for many coating jobs. Up to 1965 all these techniques were developed to maturity so that electron beam melting, welding, evaporation, and machining gained a secure position as production processes. After 1975, the industrial application of electron beam processes has been processing in microelectronics and radiation treatment of plastics and coatings were developed into full-fledged production techniques. In the 1990s, the instruments of electron beam technology had been well developed. Due to some needs in the field of space, semiconductor, many applications about alloy began to be studied. In 1991, Hiroshi [Hiroshi *et al*., 1991] used electron beam furnace to melt sponge titanium. Alec [Alec, 1992] took advantage of electron beam melting providing the incremental improvement for both titanium alloys and superalloys which we need. Tomoo [Tomoo *et al*., 1992] investigated aluminum evaporation behavior in the electron beam cold hearth remelting process. In order to clarify the quantitative effect of the beam oscillation rate on the aluminum evaporation behavior, Hideo [Hideo and Alec, 1992] melted Ti-6Al-4V alloy, developed a mathematical model on the basis of a small scale electron beam melting experiment. Schulz [Schulz, *et al*., 1995] experimented on rotating

cylindrical electron beam to deposit thermal barrier coatings, using $ZrO_2$-based ingot sources with stabilizing oxides of 6.5 and 20 wt.% $Y_2O_3$ and 25/2.5 wt.% $CeO_2/Y_2O_3$ respectively. In 2000, the direct simulation Monte Carlo method was used by Boyd [Boyd, 2000] to model the physical vapor deposition of titanium using electron beam evaporation. It is concluded that electronic energy is an important factor to consider in the modeling of flows of this nature. In the same year, the deposition of superconducting films of $YBa_2Cu_3O_{7-\delta}$ was investigated both computationally and experimentally by Fan [Fan, *et al*., 2000]. The numerical analysis and experimental studies employ DSMC method and atomic absorption spectra taken in the evaporated yttrium plume and deposited film thickness profiles. Collisions between the atoms are found to have a significant effect on the film growth rate and area of uniform deposition as the evaporation rate of yttrium increases. Powell [Powell, *et al*., 2001] also used DSMC method to compare titanium evaporating from a disk surface with ring source. Beginning from 1998, a research team led by Prof. Wadley [Wadley and Groves, 1997] at the University of Virginia designed a new physical vapor deposition technique, named for Directed Vapor Deposition (DVD). Compared with conventional electron beam physical vapor deposition, it used low vacuum electron beam evaporation in combination with a carrier gas stream to transport and vapor spray. Recently, it is highly studied, with its high rate, efficient deposition of refractory elements, alloys, and compounds onto flat or curved surfaces. Hass [Hass, *et al*., 2004] took experiments and found that the coating thickness around the circumference of a stationary, non-rotated fiber placed perpendicular to the axis of a gas jet containing aluminum atoms is sensitively dependent upon the jet's Mach number and the chamber pressure near the substrate. By employing gas jets having

low Mach numbers (< 0.1), highly uniform coating of aluminum on cylindrical fibers have been achieved without fiber rotation. DSMC simulations have been used to understand the fundamental phenomena.

## 1-4 Specific Objectives of the Thesis

Based on previous reviews, the current objectives of the thesis are summarized as follows:

(1) A DSMC code developed in MuST Lab. is used to model this rare flow field.

(2) To verify the flux distribution obeying cosine distribution.

(3) To simulate a simple case — one source in the chamber, observing the variation of density, temperature and velocity in the chamber.

(4) To contrast simulations with and without background pressure effect.

(5) To deposit the alloy Ti6Al4V and discuss the uniformity of composition and thickness on the substrate.

(6) To change some parameters to compare the uniformity with each other, making conclusions how we should adjust to obtain acceptable uniformity.

The organization of the thesis would be stated as follow: First is this introduction, and next is the numerical method. Then show the results and discussions. Finally summarize and recommend the future work.

# Chapter 2 Numerical Method

Generally, numerical methods for fluid dynamics are categorized as continuum-based and particle-based methods. Due to the expected rarefaction in the EBPVD, the Navier-Stokes equations fail to solving rarefied gas dynamics problem, current research will be investigated by DSMC method [Bird, 1994], which is a particle-based method.

The degree of rarefaction of a gas is generally expressed through the Knudsen number (Kn) which is the ratio of the mean free path $\lambda$ to the characteristic dimension L, i.e.

$$Kn = \frac{\lambda}{L} \tag{2.1}$$

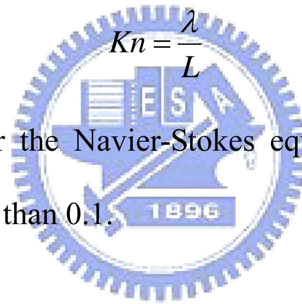

The traditional requirement for the Navier-Stokes equations to be valid is that the Knudsen number should be less than 0.1.

**2-1 DSMC Method**

The direct simulation Monte Carlo (DSMC) method is widely used as an effective numerical technique to simulate rarefied, nonequilibrium gas flow. In the DSMC method, a large number of particles are generated in the flow field to represent real physical molecules. Their initial properties are determined by the macroscopic quantities such as density, temperature and velocity, according to equilibrium distributions. The time step employed is sufficiently small so that the movement of the particles and the interaction between them can be decoupled. In each time step, the particle trajectory is computed, and its location is updated. The entire computational domain is divided into a network of

cells. Each cell serves as a separated region for the molecular interaction. A particle is only allowed to collide with another particle belonging to the same cell. Therefore, the size of the computational cell must be of the magnitude of a mean free path. Probabilities of particle collision are determined by the collision rates from kinetic theory. During each collision, modeling particles exchange momentum and energy, and chemical reactions may also take place. Once a steady state is established, time averaging is performed in each cell to evaluate the macroscopic mean values of the flow properties. Important steps of the DSMC method include setting up the initial conditions, moving all the simulated particles, indexing all the particles, colliding between particles, and sampling the particles within cells to determine the macroscopic quantities. The details of the procedures show in Fig. 2.1.

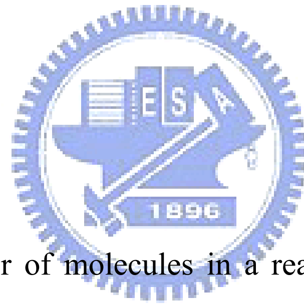
ES A 1896

**2-2 Parallel DSMC Method**

Although the large number of molecules in a real gas is replaced with a reduced number of model particles, there are still a large number of particles must be simulated, leading to tremendous computer power requirements and needing to cost a lot of computational time. As a result, parallel DSMC method is developed to solve the problem. Fig. 2.2 illustrates a simplified flow chart of the 3-D parallel DSMC method used in the current study. The DSMC algorithm is readily parallelized through physical domain decomposition. The cells of the computational grid are distributed among the processors. Each processor executes the DSMC algorithm in serial for all particles and cells in its domain. Data communication occurs when particles cross the domain (processor) boundaries and are then transferred between processors.

First, we construct an unstructured tetrahedral using a commercial meshing tool. The output grid data are then processed using a conversion program to transform them into a *globally sequential but locally unstructured mesh* data [Wu and Lian, 2003] conforming the partitioning information, as schematically shown in Fig. 2.3. In addition, a processor neighbor-identifying array is created for each processor, which is used to identify the surrounding processors due to the unstructured format of the processor distribution in the domain. The resulting *globally sequential but locally unstructured* mesh data is then imported into the parallel DSMC code.

After reading the mesh data on a master processor (cpu0), the mesh data are then distributed to all other processors according to the predetermined domain decomposition. All the particles on each processor then start to move as in sequential algorithm. The particle data are sent to a buffer and is numbered sequentially when hitting the inter-processor boundary (IPB) during its journey within a simulation time step. After all the particles on a processor are moved, the destination processor for each particle in the buffer is identified via a simple arithmetic computation, owing to the approach adopted for the cell numbering, and are then packed into arrays. Considering communication efficiency the packed arrays are then sent as a whole to its surrounding processors in turn based on the tagged numbers. Once a processor sends out all the packed arrays, it waits to receive the packed arrays from its surrounding processors in turn. This “send” and “receive” operation serves practically as a synchronization step during each simulation time step. Received particle data are then unpacked and each particle continues to finish its journey for the remaining time step. The above procedures are repeated twice since there might be some particles cross the IPB twice during a simulation time step.

After all particles on each processors have come to their final locations at the end of a time step, the program then carries out the indexing of all particles and the collisions of particles in each computational cell on each processor as usual in a sequential DSMC code. The particles in each cell are then sampled at the preset appropriate time.

Higher parallel efficiency can only be achieved if communication is minimized and the computational load is evenly distributed among processors. To minimize communication for between processors, the spatial domain decomposition should adapt according to the workload distribution as simulation continues, which requires dynamic domain decomposition. For the DSMC algorithm, the workload (or equivalently particle numbers) on each processor changes frequently, especially during the transient period of a simulation, while the workload attains a roughly constant value during steady-state sampling.

Although DSMC possesses nearly 100% parallelism (except for initialization and final output), both the values of speedup and efficiency are expected to be lower than the ideal values due to the load unbalancing and communication as mentioned previously. It is needed to make the load balanced.

**P**arallel **DS**MC **C**ode (PDSC) is the main solver used in this thesis, which utilizes unstructured tetrahedral mesh. Fig. 2.4 is the features of PDSC and brief introduction is listed in the following paragraphs.

### 2-2-1 Unstructured Tetrahedral Mesh

Reasons of PDSC using unstructured tetrahedral mesh are: (a) it can be easily used for flows with complicated boundary conditions, (b) parallel processing can be easier

implemented via graph-partitioning technique, which can handle irregular inter-processor boundary of dynamic domain decomposition, (c) it can be coupled with unstructured node-based numerical method (e.g. N-S equations).

According to these advantages of using unstructured mesh, a special particle ray-tracing technique has to be designed to efficiently track the particle movement for the special grid system, unstructured grid, which we use in the current study. Briefly speaking, the movement of a particle is determined by the velocity and initial position of the particle. If the intersecting face is an I/O boundary, the particle will be removed. If not, then process the interaction according to the specified wall boundary condition. The details of particle ray-tracing techniques of two- and three-dimensional domain are described in Ref. [Tseng, 2000; Lian, 2001].

**2-2-2 Collision Cross-Section Data**

In real molecular collision, the force between molecules is strongly repulsive at short distance and weakly attractive at larger distance. Models for analytical and numerical studies involve some degree of approximation. These models are developed to imitate the real particle collision according to experiment. There are three molecular collision models, which are the Hard Sphere (HS), Variable Hard Sphere (VHS) and Variable Soft Sphere (VSS) molecular models, in the standard DSMC method [Bird, 1994]. The total collision cross section of the hard sphere model is proportional to the square of the constant diameter. It has the advantage of easily calculated collision mechanics because of the isotropic scattering that means all directions are equally possible for the post-collision velocity in the center-mass frame of reference. But the

cross-section should vary with relative velocity in reality. The variable hard sphere (VHS) model proposes the collision diameter is a function of relative speed, which can predict the viscosity more accurately. The cross-section is determined from the viscosity coefficient, but the ratio of the momentum to the viscosity cross-section follows the hard sphere value. Thus, the variable soft sphere (VSS) model is developed to predict the correct viscosity and diffusion coefficients, which the scattering of post-collision is not isotropic anymore. The VSS model can reproduce the viscosity and diffusion coefficients correctly. The relevant parameters of using VSS model for the DSMC method can be found in Bird's book [Bird, 1994]. This reference provides some usual gaseous species. When the flow involves some special species, it has problem to obtain the relevant parameters of the VSS molecular model. To overcome this problem, a quantum chemistry method is proposed to calculate the intermolecular energy surface according to the distance between molecules [Wu and Hsu, 2003]. Then the simulated intermolecular energy potential is fitted through the Lennard-Jones (L-J) potential to obtain the constants. Based on these constants and gas kinetic theory, the transport coefficients, which are viscosity and diffusion coefficients, are derived. Finally, the parameters of the VSS model are derived by fitting these computed coefficients to those derived from the VSS model.

### 2-2-3 Pressure Boundary Treatment

In order to perform accurate simulation for inflow/outflow pressure boundaries, general procedure for treating these conditions by using the concept of particles flux conservation is developed in PDSC [Wu, *et al*., 2001]. This function is useful for applications of micro-manifold, micro-nozzle and slider air bearing.

### 2-2-4 Unstructured Adaptive Mesh with Variable Time-Step Scheme

The accuracy of a DSMC simulation is directly related to the number of simulated particles per cell throughout the cells. As the number of simulated particles increases, the statistical uncertainties of the macroscopic properties reduce due to better collision condition. The number of simulated particle per cell is shown to inversely proportional linear and square of gas density for two- and three-dimensional flows, respectively. That is, the simulated molecules are fewer in higher density regions, while lower density regions are over resolved. More computational time is spent calculating the lower density regions than is needed. A strategy to increase the computational speed without sacrificing the accuracy of the solution is to reduce the number of simulated particles by using cell/particle weighting, but maintaining near-uniform particle distribution per cell. Kannenberg and Boyd [Kannenberg and Boyd, 2000] presented strategies for efficient particle resolution in DSMC. The authors manipulated variations of particle weight, variations of time-step and grid arrangement to obtain a more uniform particle count throughout the flow field. It was shown that careless use of cell/particle weighting often introduces some detrimental effects to the statistical accuracy, which is caused by repeatedly cloning the particles in the flow field. Nevertheless, variable time-step method represents one of the simplest and most efficient ways of particle weighting that avoids the problem of particle cloning, if careful grid manipulation is done. To obtain a more uniform distribution of model particles per cell throughout the computational domain, a variable time-step scheme is highly recommended.

The number of simulated particles per cell is related to the number density, cell volume and particle weight by the following relation;

$$N_P = \frac{nV}{W_P} \tag{2.2}$$

$N_p$ is the number of simulated molecules of $p^{\text{th}}$ cell. $W_p$ is the particle weight which is defined as ratio of the number of real particles to the number of simulated molecules, and $n$ and $V$ are the number density and the volume of the computational cell, respectively. If the number density is assumed to be a constant, the simulated particle count decreases by decreasing the cell volume or increasing the particle weight. As mentioned previously, mesh refinement can help to obtain a better cell-size distribution, ideally on the order of the local mean free path. The volume of a cell can then be related to density by the fact that the mean free path is inversely proportional to the number density. Thus, the relationship between these variables is shown as Eq. (2.3),

$$\Delta x \propto \lambda \propto n^{-1} \tag{2.3}$$

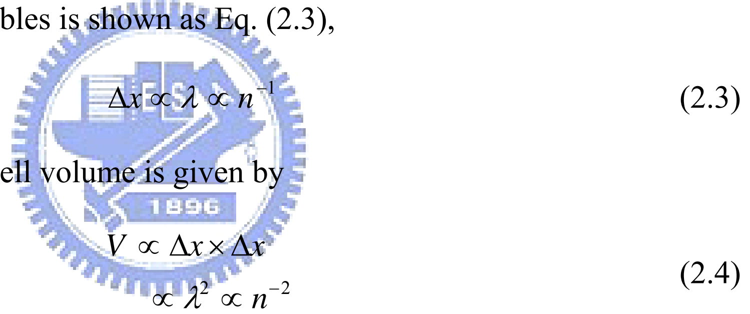

For two-dimensional flow, the cell volume is given by

$$\begin{aligned} V &\propto \Delta x \times \Delta x \\ &\propto \lambda^2 \propto n^{-2} \end{aligned} \tag{2.4}$$

For three-dimensional flow, the cell volume is given by

$$\begin{aligned} V &\propto \Delta x \times \Delta x \times \Delta x \\ &\propto \lambda^3 \propto n^{-3} \end{aligned} \tag{2.5}$$

Substituting Eqs. (2.3)~(2.5) into Eq. (2.2), give the following relation between number of simulated particles and flow density (assuming constant particle weight):

$$\begin{aligned} N_p &\propto n^{-1} \propto \Delta x \;, \quad 2D \\ N_p &\propto n^{-2} \propto \Delta x^2, \quad 3D \end{aligned} \tag{2.6}$$

According to Eq. (2.6), the number of simulated particle is inversely linear and square proportional to the number density with respect to the two- and three-dimensional flows.

That is, the lower density regions have larger simulated particle numbers and the higher density regions have fewer simulated molecular numbers. This effect is more obvious in three-dimensional simulation. This will lead to computational waste and incorrect results at lower and higher density regions, respectively. To avoid this problem, a variable time-step scheme is proposed to obtain a more uniform particle distribution as follows:

From Eq. (2.6), the density distribution is inversely proportional to the dimension of the cell. Thus, the first step of variable time-step scheme is to find out the cell, which has the minimum cell volume ($V_{\min}$), and to calculate the local time-step of the cell as Eqs. (2.7) and (2.8). The time-step is also proportional to $\Delta x$ and inversely proportional to the number density,

$$\begin{aligned}\Delta t_{\min,2D} &= \frac{\sqrt{V_{\min}}}{3\times(U_{mean}+\sqrt{2kT/m})} \propto \Delta x \propto n^{-1}, \quad 2D \\ \Delta t_{\min,3D} &= \frac{\sqrt[3]{V_{\min}}}{3\times(U_{mean}+\sqrt{2kT/m})} \propto \Delta x \propto n^{-1}, \quad 3D\end{aligned} \tag{2.7}$$

$U_{mean}$ and $\sqrt{2kT/m}$ are the mean and thermal velocity, respectively. Then, each local time-step $\Delta t_j$ of each cell can be assigned based on $\Delta t_{\min}$ and the cell volume $V_j$ as Eq. (2.8).

$$\begin{aligned}\Delta t_i &= \sqrt{\frac{V_i}{V_{\min}}} \times \Delta t_{\min,2D}, \quad 2D \\ \Delta t_i &= \sqrt[3]{\frac{V_i}{V_{\min}}} \times \Delta t_{\min,3D}, \quad 3D\end{aligned} \tag{2.8}$$

where $V_i$ and $\Delta t_i$ are the volume and local time-step of $i^{th}$ cell. Sketch of the concept of the variable time-step scheme for a simulated particle moves across the cell interface is illustrated in Fig. 2.5.

Basic idea of variable time-step method in PDSC is to enforce the flux conservation (mass, momentum and energy) of moving simulated particle when crossing the interface between two neighboring cells. If we scale the local cell time-step to the local cell size (or local mean free path), then the best way to enforce flux conservation is to change the particle weight factor without destroying or cloning the particles during particle movement across the cell interface. The cloning of particle can generally induce unpredictable random-walk effects in a statistical simulation like DSMC. One of the advantages in implementing the variable time-step scheme is to reduce both the simulated particle numbers and transient time-step to steady state, when the sampling normally starts in DSMC. This will result in appreciable time saving for the steady DSMC simulation. The net flux of the physical particles, including mass, momentum and kinetic energy, should be enforced conservation when a simulated particle crosses the cell interface from the cell 1 and to the cell 2. Thus,

$$f_1 = \frac{N_1 W_1 \Phi_1}{A \times \Delta t_1} u = f_2 = \frac{N_2 W_2 \Phi_2}{A \times \Delta t_2} u \tag{2.9}$$

where $W$'s, $\Phi$'s (=$m$, $mv$, $mv^2/2$ or other internal energy) and $\Delta t$'s are the particle weight, conserved flux quantity and time-step, respectively, and the numbers at subscript represents cell numbers. Note that $A$ represents the area of cell interface between cell 1 and 2. $N_2$ is number of the simulated particle in cell 2, which originated from cell 1. There are several choices of the corresponding parameters to satisfy Eq. (2.9), with which we can play. The best choice is to set $N_2$=1 (without particle cloning or destroy) and to keep $\Phi_1 = \Phi_2$ without changing the velocity across the cell interface, Eq. (2.9) can be rewritten as Eq. (2.10)

$$\frac{W_1}{\Delta t_1} = \frac{W_2}{\Delta t_2} \tag{2.10}$$

In other words, $\frac{W_i}{\Delta t_i}$ will be the same for all cells throughout the computational domain.

Inserting Eqs. (2.8)~(2.10) into Eq. (2.2), the number of simulated particles per cell is,

$$\begin{aligned} N_P &= \frac{nV}{W_P} \propto \frac{\Delta x^{-1} \times \Delta x^2}{\Delta t} \propto \frac{\Delta x}{\Delta t} \propto 1, \qquad 2D \\ N_P &= \frac{nV}{W_P} \propto \frac{\Delta x^{-1} \times \Delta x^3}{\Delta t} \propto \frac{\Delta x^2}{\Delta t} \propto \Delta x, \qquad 3D \end{aligned} \tag{2.11}$$

Using this approach, resulting number of simulated particles per cell for the three-dimensional flow scales with Δx ($\sim\sqrt[3]{V_c}$ , $V_c$ is the cell volume) if cell size is proportional to the local mean free path, which otherwise scales with $(\Delta x)^2$. In doing so, the simulated particle will only have to adapt its weight that is proportional to the size of time-step, which is approximately commensurable to the local mean free path if solution-based adaptive mesh is used. Of course, the remaining time for a simulated particle, when crossing cell interface, should be rescaled according to the ratio of time-steps in original and destination cells. In the PDSC, the procedure of variable time-step scheme is listed in the following;

1. Chose a minimum cell volume to calculate the reference time-step.
2. Assign the time-step for each cell based on the cell size.
3. Determine the particle weight for each cell by Eq. (2.10)
4. The time-step has to be modified if the particle crosses the cell interface.

By using this variable time-step scheme, the simulated particle number and transient time will be reduced to speed up the computing.

### 2-2-5 Parallel with Dynamic Domain Decomposition

To save the enormous computational cost of the standard DSMC code, a parallel DSMC with dynamic domain decomposition. Message passing interface (MPI) is used for data communication. This function can automatically repartition the graph domain according to the loading of each processor, which is the particle number of each cell, to achieve the load balancing of the simulation. It also can be used for other particle simulation and equation solvers.

This section presents an overview of the algorithms implemented of dynamic load decomposition scheme. The parallel performance will become worse resulting from the communication and the load unbalancing. Dynamic domain decomposition scheme for an unstructured mesh is implemented to speed up the parallel computing. Basic concept is the domain will be repartition when the loading of each processor is becoming unbalancing. The simulator aims to balance the number of particles on the sub-domains. The flowchart with dynamic domain decomposition is shown as Fig. 2.6. The procedures of the flowchart are almost the same except some processes of dynamic domain decomposition method. There are three main processes, which are decision policy for repartitioning, repartition the domain and cell/particle migration, for dynamic domain decomposition.

### 2-2-6 Conservative Weighting Scheme

When the flow involving trace particle species, the simulation needs lots of simulated particles to satisfy the DSMC limit, which will lead to immense computational time. A weighting scheme is developed to deal with this kind of flows. The basic concept

is assigning the lower weight for trace particle species to create more simulated particles. This method does not use particle cloning and destroying to avoid the statistical error.

To overcome the trace problem mentioned in the above, recently Boyd [Boyd, 1996] proposed a conservative weighting scheme, which is described briefly in the following. In this method, each species has its weighting. Non-trace and trace species have larger ($W_1$) and smaller ($W_2$) weights ($W_2/W_1 <1$), respectively. The first stage of the conservative weighting scheme is to split the particle of abundant species ($W_1$) into a particle with weight $W_2$ (trace species) and a particle with weight of $W_1$-$W_2$ when two particles (trace and abundant species) collide. Then, a collision is then performed using the conventional DSMC procedure for the two particles that have the same weight $W_2$. The final stage is to merge together the two particles that were split such that the each linear momentum in three physical directions is exactly conserved. The momentum conservative equation is shown as Eq. (2.12);

$$\begin{aligned} P_x &= W_1 m_1 u_1 + W_2 m_2 u_2 = W_1(m_1 u_1 + \phi m_2 u_2), \quad \phi = W_2/W_1 \\ &= W_1[(1-\phi)m_1 u_1 + \phi(m_1 u_1 + m_2 u_2)] \end{aligned} \tag{2.12}$$

$u_1$, $u_2$, $m_1$ and $m_2$ are the pre-collision velocities and the molecular mass of the collision partners, respectively. Eq. (2.12) means the non-trace particle ($W_1$) is split into two parts imaginatively; one particle has weighting $W_2$ and the other has weighting $W_1$-$W_2$. The first part will has elastic collision with the trace particle, but the second part remains the same situation. Thus, Eq. (2.12) can be rewritten as Eq. (2.13)

$$\begin{aligned} P_x &= W_1[(1-\phi)m_1 u_1 + \phi(m_1 u_1 + m_2 u_2)] \\ &= W_1[(1-\phi)m_1 u_1 + \phi(m_1 u_1^{'} + m_2 u_2^{'})] \end{aligned} \tag{2.13}$$

$u_1^{'}$ and $u_2^{'}$ are the post-collision velocities of the first part of non-trace particle and the

trace particle, respectively. Then the two parts of non-trace particle are merged as one particle

$$P_x = W_1[m_1 u_1'' + \phi m_2 u_2'] = W_1 m_1 u_1'' + W_2 m_2 u_2', \quad u_1'' = (1-\phi)u_1 + \phi u_1' \qquad (2.14)$$

$u_1''$ and $u_2'$ are the real final velocities of the non-trace and trace particles, respectively. The momentum is conserved by Eq.(2.12)~Eq.(2.14).

Unfortunately, it does not explicitly conserve total energy. But the energy difference (loss) caused by this split-merge process is found to be proportional to the weight ratio $W_2/W_1$ (<1). The energy lost for each collision is calculated by Eq. (2.15),

$$\begin{aligned} \Delta E = E' - E &= W_1 \frac{1}{2} m_1 [(u_1''-u_1)^2 + (v_1''-v_1)^2 + (w_1''-w_1)^2] \\ &+ W_2 \frac{1}{2} m_2 [(u_1''-u_1)^2 + (v_1''-v_1)^2 + (w_1''-w_1)^2] \\ &= W_1 \frac{1}{2} m_1 \phi (1-\phi)[(u_1 - u_1')^2 + (v_1 - v_1')^2 + (w_1 - w_1')^2] \end{aligned} \qquad (2.15)$$

Thus, the conservative weighting scheme proposed by Boyd nearly conserves total energy as this weight ratio is much smaller than unity. The split-merge process described in the above can be summarized as Figure 2.7.

It was argued that if the split-merge scheme is employed at each collision, then energy is continuously lost from the system because of energy loss. Boyd also proposed some practical remedy to keep this energy loss to a minimum by adding lost energy to the central-mass energy in a subsequent collision. In general, this energy should only be added to collisions between particles both having the maximum weight used in the simulation to keep this effect a minimum; that is, between two non-trace particles. Thus, energy conservation is essentially maintained for each iterative step of the simulation.

### 2-2-7 Molecular Chemical Reaction

PDSC also has the function to simulate flows with chemical reactions. Chemistry is important and needs to be considered when the flow velocity and temperature is very high. It has dissociation, exchange and recombination reactions in PDSC.

The difference between conventional and chemical codes is the collision partners have to calculate the reaction probability (steric factor) to determine if the chemical reaction occurs or not when two particles are chosen as collision partner. Thus, the most important part of chemical reaction is how to derive the reaction probability. The flow chart of chemistry in PDSC is shown in Fig. 2.8 and the process is described sequentially as follows:

1. Selecting two particles randomly in the current cell. The type of chemical reaction can be easily determined by these two particles.
2. Calculating the total energy and comparing with activation energy of the specific chemical reaction if this collision event has possibility to occur chemical reaction. If not, processing the normal elastic collision as usual.
3. Calculating the reaction probability according to the type of chemistry and using the Acceptant-Rejection method to determine if the chemistry occurs or not.
4. If the reaction probability is too small to process chemical reaction, the collision is processed by the elastic mechanism. But when the reaction probability is larger than a random number, that means the chemical reaction occurs and we have to assign energies, velocities and positions of product particles. For dissociation reaction, the diatomic product is dissociated as two

monatomic atoms which both have the same positions as the product. For recombination reaction, two monatomic atoms are compounded as a diatomic molecule, which position is assigned as the center point of the previous two reactants. The positions of products for exchange reaction do not change as pre-collision. No matter what chemical reaction is, the translational and internal energies are redistributed by the Larsen-Borgnakke model [Borgnakke and Larsen, 1975] and the post-collision velocity is assigned according to the post-translational energy.

# Chapter 3 Results and Discussion

### 3-1 Simulation Conditions of one source

In order to understand the transport phenomena, we simulate a simple case first, one source in the chamber. Taking computational efficiency and simulation accuracy into account, we select the quarter half sphere for simulation region. The geometry is shown in Fig. 3.1. The source is in the center of the simulation region with 200 cm in diameter. The metal put on the source is titanium.

Because we focus on evaporation behavior above the source, the unstructured mesh in the source is denser than other region. The mesh size observe the rule that it should double or triple larger than mean free path, which defined $\lambda = \frac{1}{\sqrt{2}\pi n\sigma^2}$, where $n$ is number density and $\sigma$ is collision diameter. Then, we apply DSMC code to model the flow condition. To sample the flow properties, we take an appropriate interval of time step that flow has already reach steady state and then average the flow properties by statistic concept. During each time step, motion and collisions are assumed to be decoupled such that particles are generated at the source and moved according to their velocities and boundary interactions. Collisions are calculated and particles are given new velocity.

A DSMC simulation predicts the trajectories and collisions of representative particles, each of which represents large numbers of atoms. Usually, we decide how many particles to simulate, based on how many cells in the flow condition. Around 10 or 20 particles in each cell are acceptable. Particles are introduced into the cell from the source surface at a rate given by the Langmuir equation. These particles are given a

random velocity whose magnitude follows a Maxwellian distribution (i.e. kinetic energy follows a Boltzmann distribution) such that average velocity is a function of source temperature, and whose direction follows a cosine distribution. Pairs of particles within a cell are chosen randomly, their collision probability calculated based on their relative velocities, and if a random variable is chosen which satisfies that probability, they are collided and given new velocities, which are given by various collision models. For the purpose of determining collisions and resulting velocities, particles are modeled as hard sphere. Other collision models include the variable hard sphere model, in which collision diameter depends on relative velocity, and soft sphere models involving energy transfer between kinetic energy and the internal vibrational, rotational and electronic energies. In this study, the model we select is hard sphere.

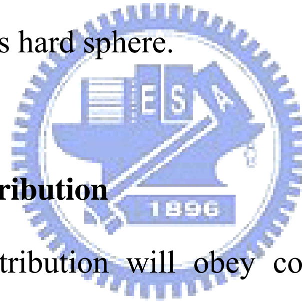


### 3-1-1 Verification of Flux Distribution

To verify if the flux distribution will obey cosine distribution, we select five different source diameters for simulation. The five diameters are 0.2 cm, 2.0 cm, 4.0 cm, 8.0 cm and 16.0 cm, which corresponding the values of $d/\lambda_0$ are 0.26, 2.61, 5.22, 10.44 and 20.89. The source temperature and vapor pressure are 2050 K and 4.5 Pa. As saying above, in the ideal condition when source size becomes smaller, the flux distribution will tend to approximate consine distribution. As a result, Fig. 3.2 shows the normalized vapor flux distributions from titanium disk sources at 2050 K with four different diameters, and $\cos(\theta)$ for reference. It has been speculated that the extent of focusing should depend only on the ratio of source diameter to equivalent mean free path $d/\lambda_0$ [Powell, 1997], as discussed in chapter 1. By using the DSMC method to calculate

vapor flux profiles in titanium evaporation, the mechanism of vapor plume focusing toward the normal has been confirmed to be based on the collisions between evaporant atoms in the dense region immediately above the source.

### 3-1-2 Variations of Inflow Field

Fig. 3.3 and Fig. 3.4 show the contour about density, temperature. The simulated results correspond to general expectation. Compared with simulation condition, the percentage of error is small. The value of density and temperature close to the source is higher than others. As far away the source, the value of density and temperature decreases gradually. From Fig. 3.5, when it comes to velocity distribution, z-directional velocity is needed to pay attention. Because of great pressure difference between source and chamber, the atoms evaporated from the source move rapidly. According to compressible fluid theorem, if there is too much pressure difference, the flow condition will become supersonic flow. As a result, the value of velocity can be calculated. Fig. 3.6 shows the velocity vector in the chamber. Obviously, the greater parts of atoms leave the source at a strongly off-normal angle.

The calculations presented here were performed under relatively clean conditions, that is, with uniform temperature distribution on the source, effects of beam scan rate ignored, and the background gas neglected. In order to make this study more closely simulate the conditions in an actual evaporation system, however, we should take these factors into consideration. For this reason, we will add the background gas effect into simulation in the next section.

### 3-1-3 Comparison of Simulations with and without Background Gas

we investigate the following cases based on dimensions that company SYSKEY provided. The chamber is shown in Fig. 3.7, with 32 cm in length, 32.5 cm in width. The height of the substrate can be adjusted upward or downward. In this study, the height of the substrate is 27.5 cm. The diameter of the substrate and source are 7.62 cm and 1.5 cm, respectively. The chamber temperature is 300 K, and source temperature 2050 K. The metal put on the source is titanium. The chamber temperature and pressure are 300 K and vacuum condition. A parameter named sticking coefficient is fixed for 1 such that the particles vaporized from the source can stick on the chamber wall or substrate completely. For the purpose of obtaining preliminary reorganization of behavior in the chamber, I take the same way of simplifying the geometry of the chamber. The simulation domain contains one source and one substrate. All of them are quarter of real body. Under the condition of vacuum in the chamber, the distribution of density, temperature and z-directional velocity are shown in Fig. 3.8. At this time we are curious that if we fill the chamber with the background gas, what will happen. From Fig. 3.9, it seems obvious to see the differences from the case which background gas is air (80% $N_2$ + 20% $O_2$), and background pressure $5\times10^{-5}$ torr. The reason why the distribution of temperature and velocity differ from the vacuum condition is that when atoms of evaporant leave the source, the background gas will be compressed. As a result, background gas will give resistance to keep evaporated atoms from going forward. Once this occurs, it will appear the phenomena of shock wave. According to compressible fluid theorem, if there is shock wave in the flow field, the temperature and pressure will increase rapidly at this shock region. Contrarily, velocity will decrease rapidly. Therefore, we can explain the sharp

change on such region above the source. Fig. 3.10 shows us the change of pressure will cause different results. As the background pressure is lower, the effect of shock wave becomes not obvious.

Fig. 3.11 shows the number of deposited atoms comparison with and without background gas. We can see that the number of deposited atoms on the same position is less when the background gas is considered. That is because the atoms in the vacuum condition will spray under faster speed and have more opportunities to deposit on the substrate.

The influence with and without background gas is studied, and the properties of distribution of energy and incident angle are now investigated. The specific cells of the substrate using for sampling unit are labeled in Fig. 3.12. As we discuss the influences on distribution of energy and incident angle due to background gas, the direct thought is that the evaporated atoms will collide with background gas unceasingly. Consequently, as evaporated atoms strike on the substrate, it is expected that energy will become smaller when velocity becomes slower. We can verify this statement from Fig. 3.13. The incident angle distribution is shown in the Fig. 3.14 as the background pressure $3.11\times10^{-5}$ torr is considered. The differences between comparing with vacuum condition are not obvious just because the pressure is too rare.

### 3-2 Simulation Conditions of Multiple Sources

The thesis objective is to model the multiple sources of EBPVD. There is a titanium alloy applied widely for semiconductor and aerospace industry based on its excellent properties. This common alloy is Ti6Al4V composed of Ti, Al and V, which the weight

ratio is about 0.9, 0.06 and 0.04, respectively. The properties of individual atom are shown in Table I. The composition of Ti6Al4V is shown in Table II [35]. Its typical physical properties and mechanical properties are shown in Table III [35] and Table IV [35].

Because we want to simulate the forming of alloy, the accurate composition deposited on the substrate is needed to control well. In order to fully mixing the evaporated atoms, the position relation between three sources is designed to triangle. The distance is 1.732 cm between two sources. Fig. 3.15 shows the relative position of three sources and substrate in the simulation domain. Once sources are heated, evaporated atoms will diffuse everywhere. Fig. 3.16 shows the position of evaporated atoms at a specific steady time step.

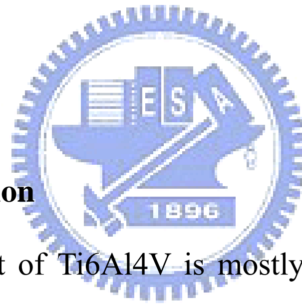

### 3-2-1 Uniformity of Composition

From Table II, the content of Ti6Al4V is mostly composed of Ti, Al and V. The reasonable range of weight ratio of aluminum is from 0.055 to 0.0676, and vanadium is from 0.035 to 0.045. If we want to deposit the alloy which corresponds to composition like that, the number ratio of individual atoms evaporated from the source should also correspond to the ratio described above. From the Fig. 3.17[Powell, 1997], we can calculate the number of atom of each evaporant according to evaporation rate by assigning source temperature. In this study, as background pressure is $3.11\times10^{-5}$ torr, the source temperature of titanium, aluminum and vanadium is set 2000℃, 1000℃ and 1880℃. The deposited distributions of individual evaporated atom are shown in Fig. 3.18. We can see the value of distributions falling in the acceptable range. More strictly, we set

some value as a benchmark to show the distribution of error percentage, as displayed in the Fig. 3.19. These values for titanium, aluminum and vanadium are 0.9, 0.06 and 0.04, respectively. As a result, we can use the same way to show the uniformity of composition in the following case.

**3-2-2 Uniformity of Thickness**

In addition to discuss the uniformity of composition, another subject we need to focus on is the uniformity of thickness. The uniform thickness on the substrate is a significant factor in the semiconductor. Nowadays, for the purpose of reducing cost, the semiconductor manufacturers are making efforts in developing larger wafer's dimension. Therefore, the uniformity of thickness will relate to the yield of product directly.

The Ti6Al4V alloy is mostly composed of titanium. Based on this reason, we suppose that the crystal lattice structure of Ti6Al4V will be the same with titanium. And the crystal lattice structure of titanium is Hexagonal Closest Packing (HCP). The method to calculate the thickness is based on the equation:

$$thickness = \frac{N_{tot}}{\frac{A}{A_{cls}} \times n} \times c \times W_i \tag{3.1}$$

where $N_{tot}$ is the total deposited particles in a unit cell, $A$ is the area of a unit cell, $W_i$ is the particle weight for each cell $i$, $A_{cls}$ and $c$ is the bottom area and height of the crystal lattice structure, $n_{cls}$ is the lattice points per crystal lattice structure. The value of $\frac{c}{a}$ for titanium is 1.586, where $a$ is the distance between adjacent lattice points in the basal plane.

The simulation condition is the same described in the last section. The sample starts from steady condition. It takes 36000 time step in total. The distribution of thickness on the substrate is shown in the Fig. 3.20.

### 3-2-3 Growth Rate

The growth rate is governed by other process parameters such as evaporation rate, background pressure, substrate temperature, and so on. The deposited thickness is calculated based on crystal lattice structure. We gather statistics at time step 5000, 15000, 25000 and 35000. The performance coefficients are identical to the condition described above. Fig. 3.21 shows the distributions of growth rate in the period that we assign. The unit of growth rate here is m/s. We can see that the growth rate does not change obviously because it has already reached the steady condition in the chamber when gathering statistics.

1896

## 3-3 Uniformity Discussion of Different Parameters

In this section, we try to change some parameters to discuss the uniformity problem. The uniformity of composition and thickness is the subjects that we need to compare. The parameters are inclusive of the altitude of the substrate, background pressure and distance between the sources. For each case, we will show the table listed maximum value, minimum value and average value of composition of Ti6Al4V. We also select different error percentages to obtain the ratio of acceptable value to total value. The acceptable value is defined that if it is in the interval of the error percentage we assign. The calculated results are also listed in the same table. The error percentage of titanium,

aluminum, vanadium and thickness is assigned as ±0.2%, ±1.5%, ±2% and ±10%, respectively.

### 3-3-1 Altitude of the Substrate

Contrasted with the original simulated case that the substrate is located at a height of 27.5cm, we try to adjust the altitude of the substrate for the two cases of 10 cm and 40 cm. In the Fig. 3.22 we show the composition and thickness to compare with each other. All of the performance coefficients are the same. Table V shows the relevant value on the substrate for each case.

We can see that the distribution of composition will be better when the substrate is located at appropriate altitude. In other words, the altitude of the substrate can not be neither too high nor too low. The appropriate altitude should be decided according to experimental results. On the other side, the growth rate becomes slower because of the increasing altitude.

### 3-3-2 Background Pressure

As discussed if the background pressure will make influences on composition and thickness, we select three different background pressures to check it. The simulated background pressure is $5\times10^{-5}$ torr, $5\times10^{-6}$ torr and vacuum. The composition and thickness are shown in the Fig. 3.23.

It seems that the distribution of composition will be more uniform when the background pressure is rare. On the other hand, the background pressure effect doesn't make more influence on the distribution of thickness. Table VI shows the relevant value

on the substrate for each case.

### 3-3-3 Distance between the Sources

Another parameter we need to discuss is the distance between the sources. There are three cases which the distance is 1.732 cm, 4.330 cm and 6.928 cm, respectively. The results are shown in the Fig. 3.24.

We observe that the composition of aluminum and vanadium exceeds the expected value of Ti6Al4V gradually when the distance between sources is farther. The thickness is also thinner due to evaporated characteristic. Table VII shows the relevant value on the substrate for each case.

# Chapter 4 Conclusions

## 4-1 Summary

The current study carries out the simulations of electron beam physical vapor deposition using direct simulation Monte Carlo method. Due to the demand for highly vacuum environment, background pressure is an important factor that it is worthy to study the effects on the deposited reaction. In the chapter three, we show the reactions and results that the background pressure is considered. It seems that the results correspond to our previous expectations that the depositions are steadier when environment is rare in the chamber. We can verify from the uniformity discussions.

Another subject in this study is uniformity of composition and thickness by changing some parameters. These parameters we adjust are the altitude of substrate, background pressure and distance between the sources. As the EBPVD theorem saying that we can obtain uniform composition and thickness by mixing the evaporated atoms well.

The major findings of the current research are summarized as follows:

1. The tendency of simulated flux distribution will be toward the $\cos\theta$ distribution as $d/\lambda_0$ decreases approaching zero.
2. Background gas will cause the appearance of shock wave phenomena. It is a significant factor that will influence the properties of flow field in the chamber.
3. If there is background gas in the chamber, the number of deposited particle on the substrate is less.
4. The particles' energy is larger in the vacuum condition, but incident angle is almost the same compared with the environment of rare flow field.

5. It will obtain better uniformity of composition at appropriate distance between the source and substrate.
6. To compare with each other under the circumstance of high vacuum environment, the uniformity will have minor differences.
7. As increasing the distance between the sources, the composition of Al and V will exceed the upper bound of composition of Ti6Al4V gradually.

**4-2 Recommendation**

As completing simulation condition described above, we can work further for the following items:

(1) To change different combinations of temperature of three evaporants, comparing the uniformity of composition and thickness.

(2) In order to simulate the reactions between atoms close to the realistic condition, variable soft sphere model is recommended.

(3) To modify uniform temperature on the source with source temperature distribution.

(4) The effect of recondensation on evaporation rate makes influences on uniformity.

(5) Cluster growth process.

(6) Experimental data used for verifying the simulation results.

# References

[1] Alec MITCHELL, "Melting and Refining of Superalloys and Titanium Alloys", ISIJ International, 32, pp. 557-562, 1992.

[2] Bakish, R., editor. Proc. Electron Beam Melting and Refining State of the Art, Reno, Nevada, October 1995. Bakish Materials Corporation.

[3] Bellot, J. P., Hess, E., Hans, S. and Ablitzer, D., "A Comprehensive Simulation of the Electron Beam Cold Hearth Refining of Titanium Alloy", In Alec Mitchell and Philippe Auburtin, editors, Proc. 1997 Int'l. Symp. on Liquid Metal Processing and Casting, pp. 166-187, Santa Fe, February 1997. American Vacuum Society.

[4] Bellot, J. P., Floris, E., Jardy, A. and Ablitzer, D., "Numerical Simulation of the E.B.C.H.R. Process", In R. Bakish, editor, Proc. Electron Beam Melting and Refining State of the Art, pp. 139-152, Reno, Nevada, November 1993. Bakish Materials Corporation.

[5] Bird, G. A., "Molecular Gas Dynamics and the Direct Simulation of Gas Flows", Oxford University Press, New York, 1994.

[6] Borgnakke, C. and Larsen, P. S., "Statistical Collision Model for Monte Carlo Simulation of Polyatomic Gas Mixture", Journal of Computational Physics, 18, pp. 405-420, 1975.

[7] Boyd, I. D., Balakrishnan, J. and Braun, D. G., "Monte Carlo Simulation of Vapor Transport in Physical Vapor Deposition of Titanium", Journal of Vacuum Science and Technology A, 18, pp. 907-916, 2000.

[8] Boyd, I. D., "Conservative Species Weighting Scheme for the Direct Simulation

Monte Carlo Method", Journal of Thermophysics and Heat Transfer, 10, pp. 579-585, 1996.

[9] Brandes, E., editor, "Smithells Metals Reference Book", Butterworth & Co., Boston, sixth edition, 1983.

[10] Cron, M. and Adams, C. M., "Controlled Electron Beam Co-Deposition of Copper Nickel Films", Journal of Materials Science, 4, pp. 252-258, 1969.

[11] DeMasi-Marcin, J. T. and Gupta, D. K., "Protective Coatings in the Gas Turbine Engine", Surface and Coatings Technology, 68/69, pp. 1-9, 1994.

[12] Fan, J., Boyd, I. D. and Shelton, C., "Monte Carlo Modeling of Electron Beam Physical Vapor Deposition of Yttrium", Journal of Vacuum Science and Technology A, 18, pp. 2937-2945, 2000.

[13] Gilbaud, D., "Effect of Melt Surface Depression on the Vaporization Rate of a Metal Heated by an Electron Beam", In R. Bakish, editor, Proc. Electron Beam Melting and Refining State of the Art, pp. 227-242, Reno, Nevada, November 1995. Bakish Materials Corporation.

[14] Hass, D. D., Marciano, Y. and Wadley, H. N. G., "Physical Vapor Deposition on Cylindrical Substrates", Surface and Coatings Technology, 185, pp.283-291, 2004.

[15] Hideo NAKAMURA and Alec MITCHELL, "The Effect of Beam Oscillation Rate on Al Evaporation from a Ti-6Al-4V Alloy in the Electron Beam Melting Process", ISIJ International, 32, pp. 583-592, 1992.

[16] Hiroshi KANAYAMA, Tatsuhiko KUSAMICHI, Tetsuhiro MURAOKA, Toshio ONOUYE and Takashi NISHIMURA, "Electron Beam Melting of Sponge Titanium", ISIJ International, 31, pp. 906-914, 1991.

[17] Kannenberg, K. and Boyd, I. D., “Strategies for Efficient Particle Resolution in the Direct Simulation Monte Carlo Method”, Journal of Computational Physics, 157, pp. 727-745, 2000.

[18] Lian, Y.-Y., “Parallel Three-Dimensional Direct Simulation Monte Carlo Method and Its Applications”, Mechanical Engineering, National Chiao-Tung University, Taiwan, Master Thesis, 2001.

[19] Powell, A. C., “Transport Phenomena in Electron Beam Melting and Evaporation”, Massachusetts Institute of Technology, Department of Materials Science and Engineering, Ph.D thesis, 1997.

[20] Powell, A., Minson, P., Trapaga, G. and Pal, U., “Mathematical Modeling of Vapor-Plume Focusing in Electron-Beam Evaporation”, Metallurgical and Materials Transactions, 32A, pp. 1959-1966, 2001.

[21] Schiller, S., Heisig, U. and Panzer, S., “Electron Beam Technology”, John Wiley & Sons, New York, 1982.

[22] Schulz, U., Fritscher, K. and Peters, M., “EB-PVD Y2O3- and CeO2/Y2O3-Stabilized Zirconia Thermal Barrier Coatings — Crystal Habit and Phase Composition”, Surface and Coatings Technology, 82, pp. 259-269, 1995.

[23] Stohr, J. A., “Vacuum Welding by Electron Beam”, Nuclear Power, 3, pp. 272-274, 1958.

[24] Storer, J., “Electron Beam Deposition for the Fabrication of Titanium MMCs”, In R. Bakish, editor, Proc. Electron Beam Melting and Refining State of the Art, pp. 235-245, Reno, Nevada, November 1993. Bakish Materials Corporation.

[25] Storer, J., “Update on Metal Matrix Composites Produced by Electron Beam

Evaporation", In R. Bakish, editor, Proc. Electron Beam Melting and Refining State of the Art, pp. 177-181, Reno, Nevada, November 1996. Bakish Materials Corporation.

[26] Tran Kong, T. and Bird, G. A., "One-Dimensional Outgassing Problem", Physics of Fluids, 21, pp. 327-333, 1978.

[27] Tripp, D., Cockcroft, S. and Mitchell, A., "The Effect of Pressure on Power Transfer in Electron Beam Remelting", In R. Bakish, editor, Proc. Electron Beam Melting and Refining State of the Art, pp. 127-138, Reno, Nevada, November 1993. Bakish Materials Corporation.

[28] Tomoo ISAWA, Hideo NAKAMURA and Katsuhiko MURAKAMI, "Aluminum Evaporation from Titanium Alloys in EB Heart Melting Process", ISIJ International, 32, pp. 607-615, 1992.

[29] Tseng, K.-C., "Analysis of Micro-scale Gas Flows with Pressure Boundaries Using the Direct Simulation Monte Carlo Method", Mechanical Engineering, National Chiao-Tung University, Taiwan, Master Thesis, 2000.

[30] Wadley, H.N.G. and Groves, J. F., "Monte Carlo Modeling of Atom Transport During Directed Vapor Deposition", Materials Research Society Symposium - Proceedings, Thin Films - Structure and Morphology, 441, pp. 541-548, 1997.

[31] Wolf, S. and Rauber, R. N., "Process Technology", Volume 1 of Silicon Processing for the VLSI Era, Lattice Press, Sunset Beach, 1986.

[32] Wu, J.-S. and Hsu Y.-L., "Derivation of Variable Soft Sphere Model Parameters in Direct-Simulation Monte Carlo Method Using Quantum Chemistry Computation", Japanese Journal of Applied Physics, 42, pp. 7574-7575, 2003.

[33] Wu, J.-S and Lian, Y.-Y., “Parallel Three Dimensional Direct Simulation Monte Carlo Method and Its Applications”, Computers & Fluids, 32, pp. 1133-1160, 2003.

[34] Wu, J.-S., *et al*., “Pressure Boundary Treatment In Micromechanical Devices Using Direct Simulation Monte Carlo Method”, JSME International Journal, Series B, 44, pp.439-450, 2001.

[35] http://www.azom.com/details.asp?ArticleID=1547

# Appendix A

The Peclet number for heat transfer is derived from the ratio of convective to conductive terms in the energy equation, and thus gives a rough measure of which is more important in a heat transfer problem. When it is much less than one, conduction can be said to dominate; when much greater than one, convection is more important. Because the ratio of interest is that of horizontal convection to vertical conduction, the following modified version of the Peclet number is proposed:

$$Pe = \frac{u_x \Delta z^2}{\Delta x \alpha} \tag{A.1}$$

where $u_x$ is the melt flow velocity along the surface and $\Delta x$ and $\Delta z$ are the horizontal and vertical length scales of the problem. The horizontal length scale is the spot radius, and the vertical length scale can be approximated by the penetration depth of temperature fluctuations given by $2\sqrt{\alpha / f}$ .

To approximate transient surface velocity, one must use the expression for Marangoni shear $\tau_{zx}$ due to the temperature rise near the beam given by

$$\tau_{zx} = \frac{d\sigma}{dT}\frac{\partial T}{\partial x} \tag{A.2}$$

where $\sigma$ here is the surface tension and the temperature gradient is approximated as the maximum centerline temperature rise $\Delta T_{\max}$ (given by equation A.10, appendix B) divided by spot radius. One may then apply the constant flux diffusion equation solution from appendix B (equation A.8) to fluid flow, where momentum flux is given by shear $\tau_{zx}$, which gives

$$u_x = \frac{\tau_{zx}}{\mu}\left[2\sqrt{\frac{\mu t}{\pi\rho}}e^{-\frac{\rho z^2}{4\mu t}} - z\,erfc\left(\frac{z}{2}\sqrt{\frac{\rho}{\mu t}}\right)\right] \tag{A.3}$$

Using the beam dwell time $R/Lf$ as our reference time, the surface velocity will simply be

$$u_x = 2\tau_{zx}\sqrt{\frac{R}{\pi\rho\mu Lf}} \tag{A.4}$$

Inserting the shear stress given by equation A.2 into this velocity expression, and the resulting velocity into equation A.1, giving the conclusion

$$Pe = 8\frac{d\sigma}{dT}\frac{\Delta T_{\max}}{R}\sqrt{\frac{R}{\pi\rho\mu Lf}}\frac{1}{Rf} \tag{A.5}$$

$$= \frac{16\sqrt{2}P(d\sigma/dT)}{\pi^2\rho LR^3 f^2\sqrt{k\mu c_p}} \tag{A.6}$$

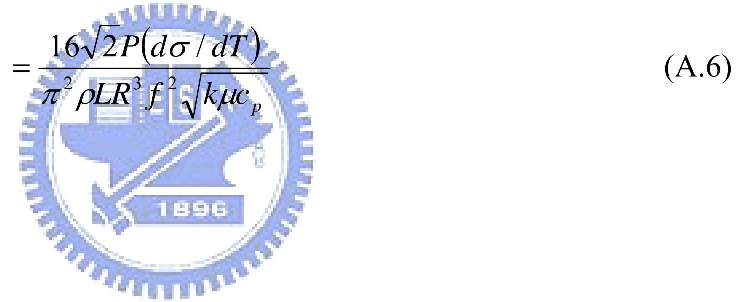

# Appendix B

To estimate the temperature rise during the dwell time of the beam, one can solve the one-dimensional heat conduction equation

$$\frac{\partial T}{\partial t} = \alpha \frac{\partial^2 T}{\partial z^2} + \frac{\dot{q}}{\rho c_p} \tag{A.7}$$

with initial condition $t = 0 \Rightarrow T = T_0$ and boundary conditions $z = 0 \Rightarrow -k\frac{\partial T}{\partial z} = q_0$ and $z \to \infty \Rightarrow T = T_0$ ( $z$ is depth into the melt), which gives the solution

$$T = T_0 + \frac{q_0}{k}\left[2\sqrt{\frac{\alpha t}{\pi}}\exp\left(-\frac{z^2}{4\alpha t}\right) - z\left(1 - erf\,\frac{z}{2\sqrt{\alpha t}}\right)\right] \tag{A.8}$$

The beam is treated as a constant heat source with surface flux $q_0 = \frac{P}{\pi R^2}$ (from the equation $q = \frac{P}{\pi R^2}\exp\left(-\frac{r^2}{R^2}\right)$) and centerline dwell time $\Delta t = 2R / Lf$ where $L$ is the pattern length and $f$ the scan frequency. Therefore, the maximum surface temperature rise along the beam centerline is

$$\Delta T_{\max} = \frac{2P}{\pi R^2 k}\left(\frac{2\alpha R}{\pi L f}\right)^{1/2} \tag{A.9}$$

$$= \frac{P}{\sqrt{k\rho c_p L f}}\left(\frac{2}{\pi R}\right)^{3/2} \tag{A.10}$$

Because this expression does not consider the gaussian nature of the beam, and does not account for radiative and evaporative heat losses, it is an overestimate of the temperature rise.

# Tables

Table I. The properties of Ti, Al, V.

| Name, Symbol, Number | titanium, Ti, 22 | aluminum, Al, 13 | vanadium, V, 23 |
|---|---|---|---|
| Group, Period, Block | 4, 4, d | 13, 3, p | 5, 4, d |
| Crystal structure | hexagonal | cubic face centered | cubic body centered |
| Atomic radius | 140 pm | 125 pm | 135 pm |
| Atomic mass | 47.867 g/mol | 26.9815386 g/mol | 50.9415 g/mol |
| Density | 4.506 $g/cm^3$ | 2.70 $g/cm^3$ | 6.0 $g/cm^3$ |
| Electron configuration | [Ar] $3d^2$ $4s^2$ | [Ne] $3s^2$ $3p^1$ | [Ar] $3d^3$ $4s^2$ |
| Melting point | 1941 K | 933.47 K | 2183 K |
| Phase | solid | solid | solid |

Table II. The composition of Ti6Al4V

| | CONTENT |
|---|---|
| C | <0.08% |
| Fe | <0.25% |
| $N_2$ | <0.05% |
| $O_2$ | <0.2% |
| Al | 5.5-6.76% |
| V | 3.5-4.5% |
| $H_2$(sheet) | <0.015% |
| $H_2$(bar) | <0.0125% |
| $H_2$(billet) | <0.01% |
| Ti | Balance |

Table III. Typical physical properties for Ti6Al4V.

| PROPERTY | TYPICAL VALUE |
|---|---|
| Density g/cm$^3$ (lb/ cu in) | 4.42 (0.159) |
| Melting Range °C±15°C (°F) | 1649 (3000) |
| Specific Heat J/kg.°C (BTU/lb/°F) | 560 (0.134) |
| Volume Electrical Resistivity ohm.cm (ohm.in) | 170 (67) |
| Thermal Conductivity W/m.K (BTU/ft.h.°F) | 7.2 (67) |
| Mean Co-Efficient of Thermal Expansion 0-100°C /°C (0-212°F /°F) | 8.6x10$^{-6}$ (4.8) |
| Mean Co-Efficient of Thermal Expansion 0-300°C /°C (0-572°F /°F) | 9.2x10$^{-6}$ (5.1) |
| Beta Transus °C±15°C (°F) | 999 (1830) |

Table IV. Typical mechanical properties for Ti6Al4V.

| PROPERTY | MINIMUM | TYPICAL VALUE |
| --- | --- | --- |
| Tensile Strength MPa (ksi) | 897 (130) | 1000 (145) |
| 0.2% Proof Stress MPa (ksi) | 828 (120) | 910 (132) |
| Elongation Over 2 Inches % | 10 | 18 |
| Reduction in Area % | 20 | |
| Elastic Modulus GPa (Msi) | | 114 (17) |
| Hardness Rockwell C | | 36 |
| Specified Bend Radius <0.070 in x Thickness | | 4.5 |
| Specified Bend Radius >0.070 in x Thickness | | 5.0 |
| Welded Bend Radius x Thickness | 6 | |
| Charpy, V-Notch Impact J (ft.lbf) | | 24 (18) |

Table V. The relevant values of Ti6Al4V compared with different altitude of the substrate: (a) 10 cm ; (b) 27.5 cm ; (c) 40 cm.

| | Maximum | Minimum | Average | Acceptable ratio |
|---|---|---|---|---|
| Ti | 0.8969262 | 0.8895243 | 0.8930359 | 0.5166667 |
| Al | 6.7761280E-02 | 6.3346483E-02 | 6.5553702E-02 | 0.4500000 |
| V | 4.2944506E-02 | 3.9722294E-02 | 4.1410439E-02 | 0.6333333 |
| Thickness(nm) | 30.143852 | 15.649038 | 21.236644 | 0.5500000 |

(a)

| | Maximum | Minimum | Average | Acceptable ratio |
|---|---|---|---|---|
| Ti | 0.8999392 | 0.8952078 | 0.8975889 | 0.8833333 |
| Al | 6.4780384E-02 | 6.1212711E-02 | 6.2680699E-02 | 0.8166667 |
| V | 4.1203082E-02 | 3.7962511E-02 | 3.9730396E-02 | 0.7500000 |
| Thickness(nm) | 4.6865596 | 3.1084202 | 3.7459880 | 0.7000000 |

(b)

| | Maximum | Minimum | Average | Acceptable ratio |
|---|---|---|---|---|
| Ti | 0.9018313 | 0.8946580 | 0.8975435 | 0.8500000 |
| Al | 6.5985218E-02 | 5.9271228E-02 | 6.2852316E-02 | 0.5833333 |
| V | 4.1586936E-02 | 3.7352987E-02 | 3.9604116E-02 | 0.6166667 |
| Thickness(nm) | 2.2513418 | 1.5063452 | 1.8192412 | 0.7833334 |

(c)

Table VI. The relevant values of Ti6Al4V compared with different pressure in the chamber: (a) $5\times10^{-5}$ torr ; (b) $5\times10^{-6}$ torr ; (c) vacuum.

| | Maximum | Minimum | Average | Acceptable ratio |
|---|---|---|---|---|
| Ti | 0.8994763 | 0.8944911 | 0.8974000 | 0.8500000 |
| Al | 6.5057889E-02 | 6.0450226E-02 | 6.2877662E-02 | 0.6833333 |
| V | 4.1000150E-02 | 3.7529990E-02 | 3.9722379E-02 | 0.7666667 |
| Thickness(nm) | 4.7098676 | 3.0981182 | 3.7469472 | 0.6833333 |

(a)

| | Maximum | Minimum | Average | Acceptable ratio |
|---|---|---|---|---|
| Ti | 0.9016619 | 0.8949397 | 0.8976156 | 0.8833333 |
| Al | 6.5159686E-02 | 6.0712483E-02 | 6.2711656E-02 | 0.7666667 |
| V | 4.1075449E-02 | 3.7580859E-02 | 3.9672747E-02 | 0.7166666 |
| Thickness(nm) | 4.6932973 | 3.1256890 | 3.7502526 | 0.7000000 |

(b)

| | Maximum | Minimum | Average | Acceptable ratio |
|---|---|---|---|---|
| Ti | 0.9004977 | 0.8945116 | 0.8975023 | 0.8333333 |
| Al | 6.5024279E-02 | 6.1098572E-02 | 6.2862754E-02 | 0.8166667 |
| V | 4.1686617E-02 | 3.7523944E-02 | 3.9634921E-02 | 0.5833333 |
| Thickness(nm) | 4.6887019 | 3.1006788 | 3.7491774 | 0.7000000 |

(c)

Table VII. The relevant values of Ti6Al4V compared with different distances between the sources: (a) 1.732 cm ; (b) 4.330 cm ; (c) 6.928 cm.

| | Maximum | Minimum | Average | Acceptable ratio |
|---|---|---|---|---|
| Ti | 0.8999392 | 0.8952078 | 0.8975889 | 0.8833333 |
| Al | 6.4780384E-02 | 6.1212711E-02 | 6.2680699E-02 | 0.8166667 |
| V | 4.1203082E-02 | 3.7962511E-02 | 3.9730396E-02 | 0.7500000 |
| Thickness(nm) | 4.6865596 | 3.1084202 | 3.7459880 | 0.7000000 |

(a)

| | Maximum | Minimum | Average | Acceptable ratio |
|---|---|---|---|---|
| Ti | 0.8952824 | 0.8906804 | 0.8932091 | 0.9166667 |
| Al | 6.7737736E-02 | 6.3664123E-02 | 6.5459445E-02 | 0.8166667 |
| V | 4.3435723E-02 | 4.0098816E-02 | 4.1331455E-02 | 0.8333333 |
| Thickness(nm) | 4.3954760 | 2.9617002 | 3.5538856 | 0.7333333 |

(b)

| | Maximum | Minimum | Average | Acceptable ratio |
|---|---|---|---|---|
| Ti | 0.8931664 | 0.8882905 | 0.8910138 | 0.9166667 |
| Al | 6.8866223E-02 | 6.5300256E-02 | 6.6667311E-02 | 0.7666667 |
| V | 4.3634392E-02 | 4.0418547E-02 | 4.2318914E-02 | 0.7333333 |
| Thickness(nm) | 4.2402091 | 2.8831408 | 3.4465084 | 0.7166666 |

(c)

## Figures

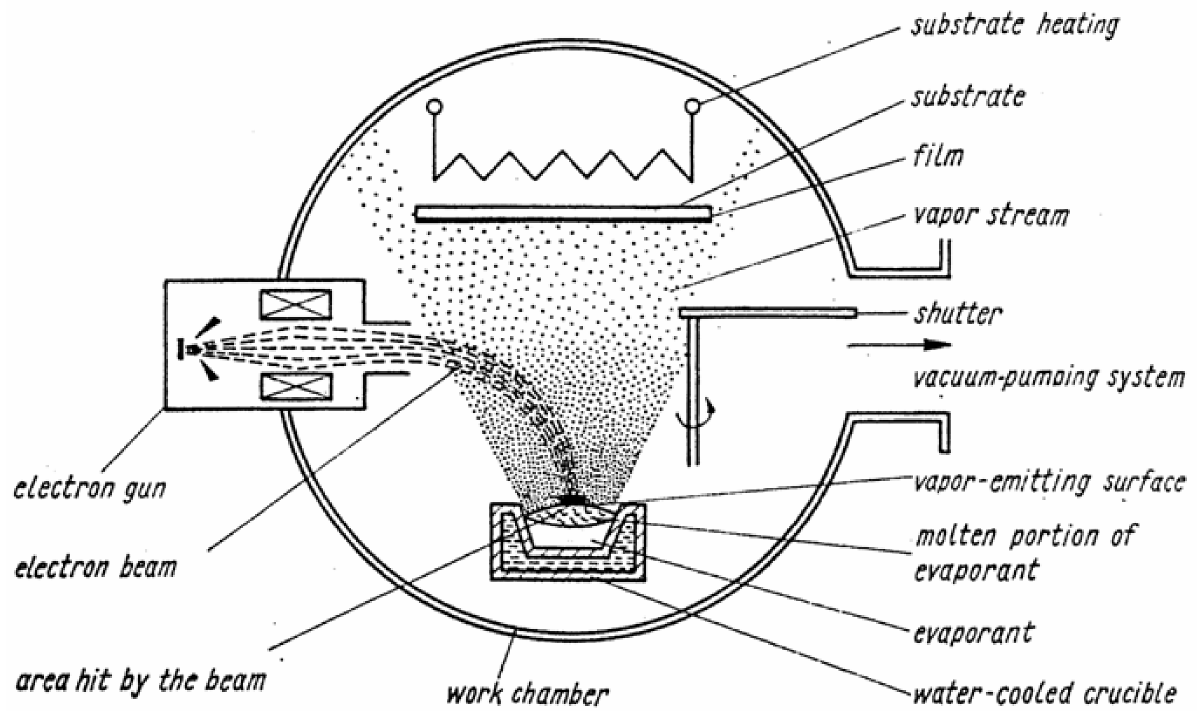


Fig. 1.1 Principle of electron beam evaporation. [Schiller, *et al.*,1982]

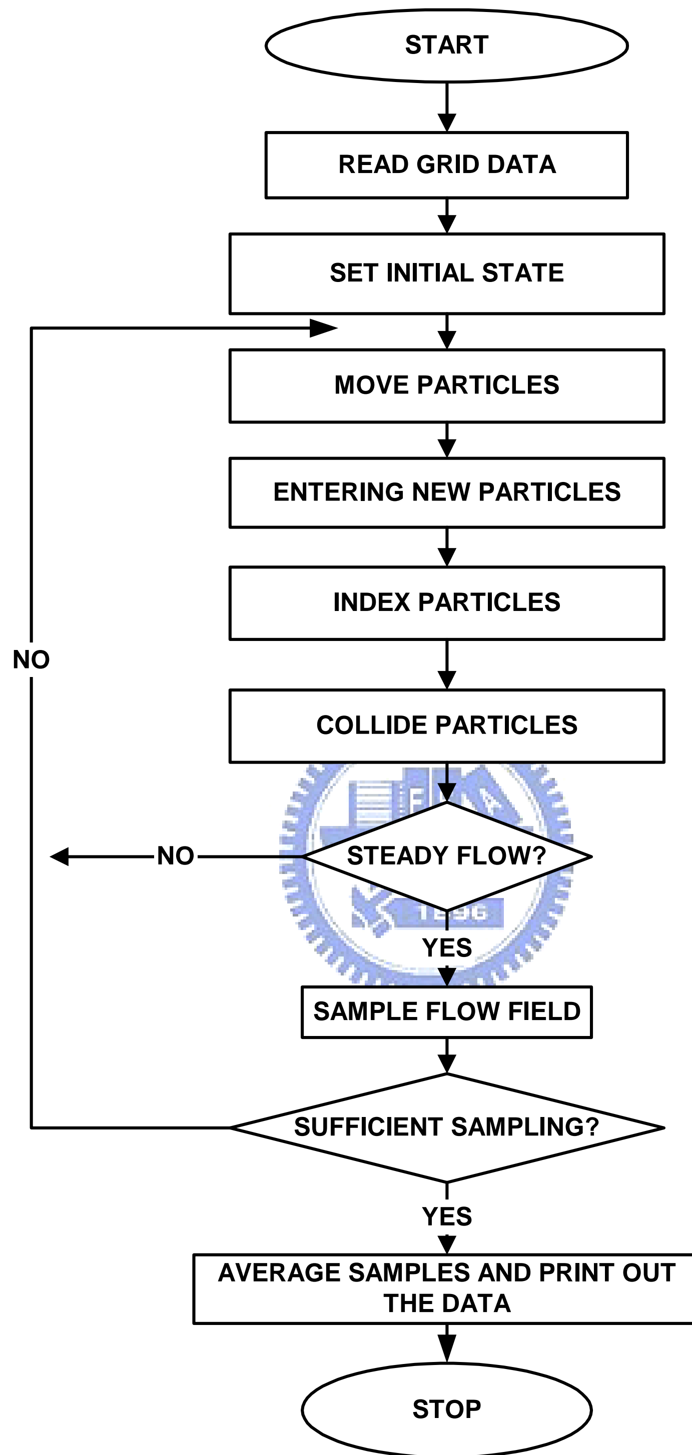


Fig. 2.1 Conventional DSMC flow chart.

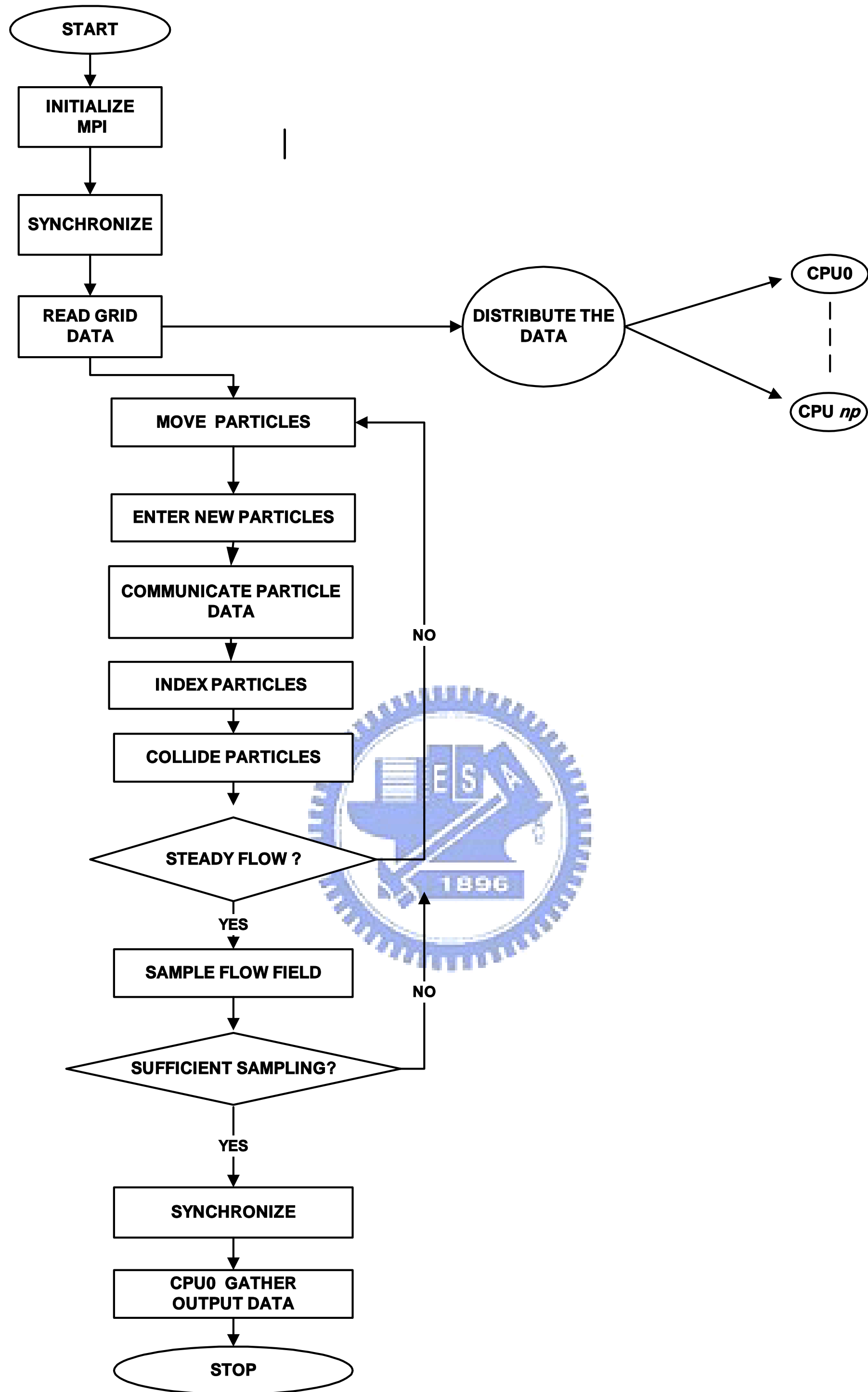


Fig. 2.2 Simplified flow chart of the parallel DSMC method for np processors.

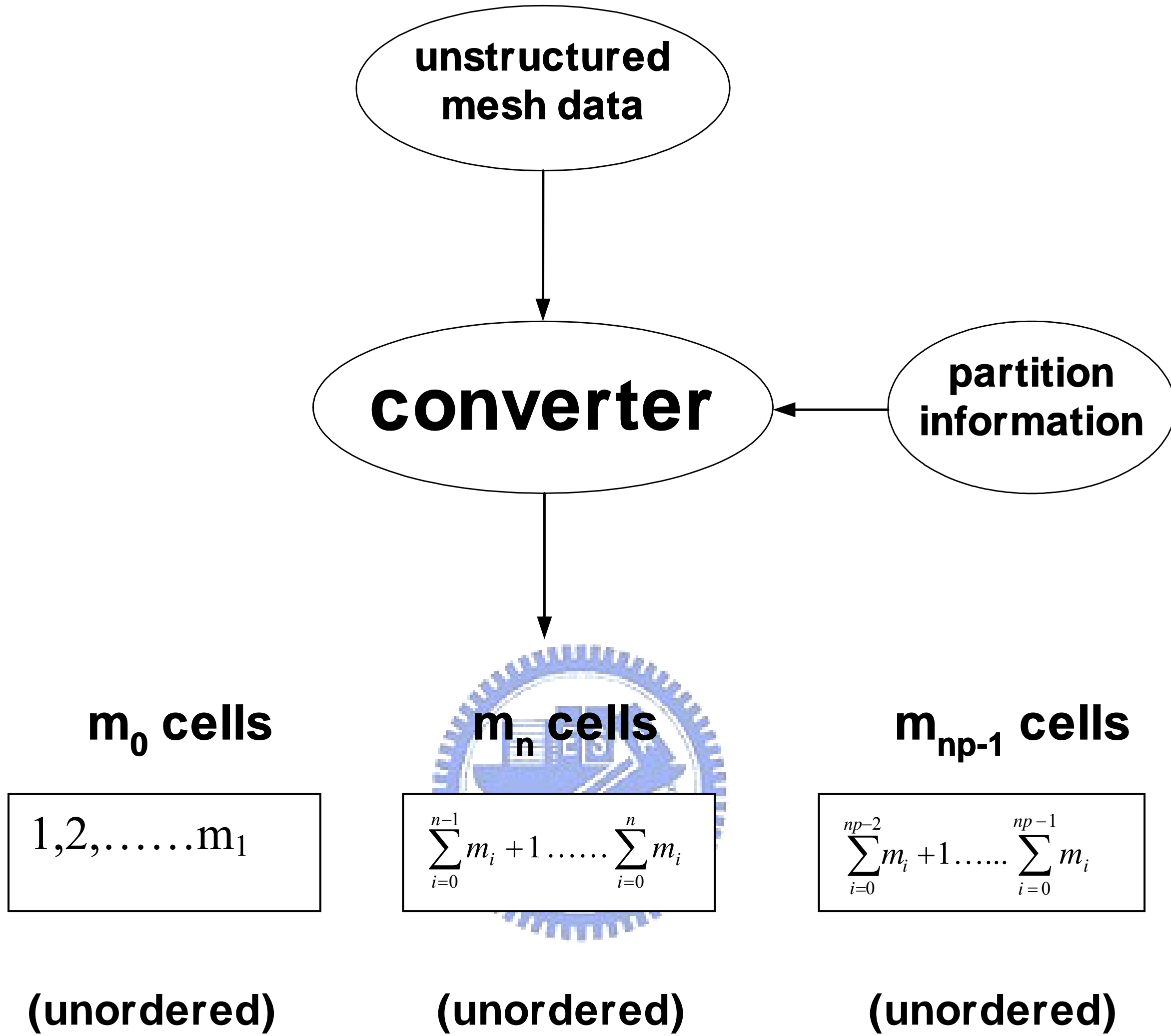


Fig. 2.3 Schematic diagram of the proposed cell numbering scheme.

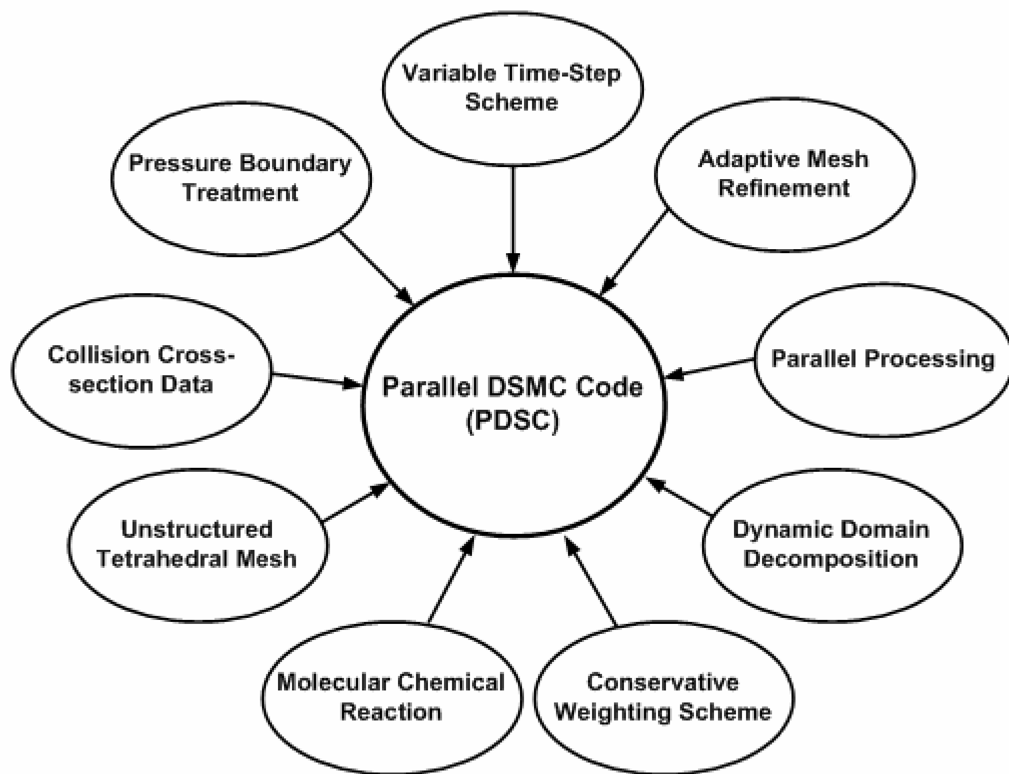


Fig. 2.4 The additional schemes in the parallel DSMC code.

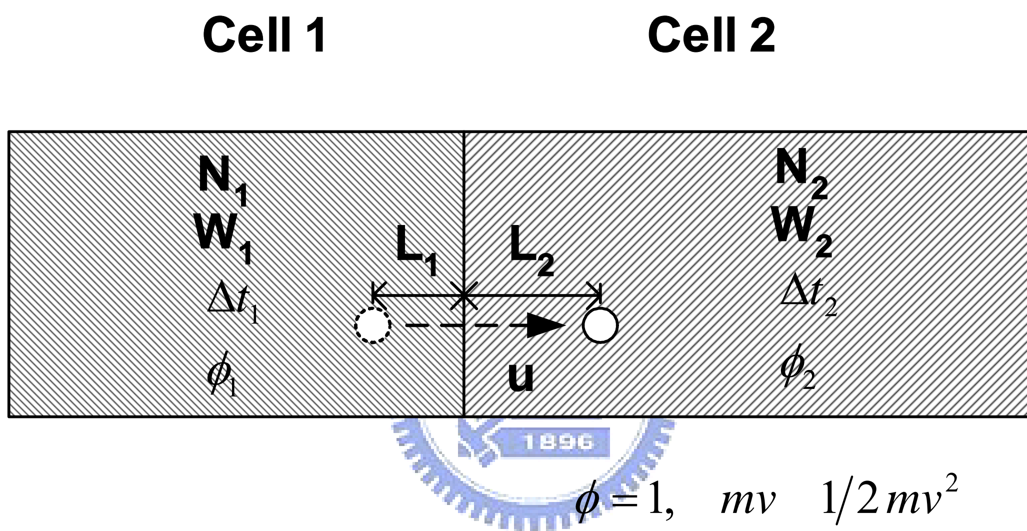


Fig. 2.5 Sketch of the concept of variable time step scheme.

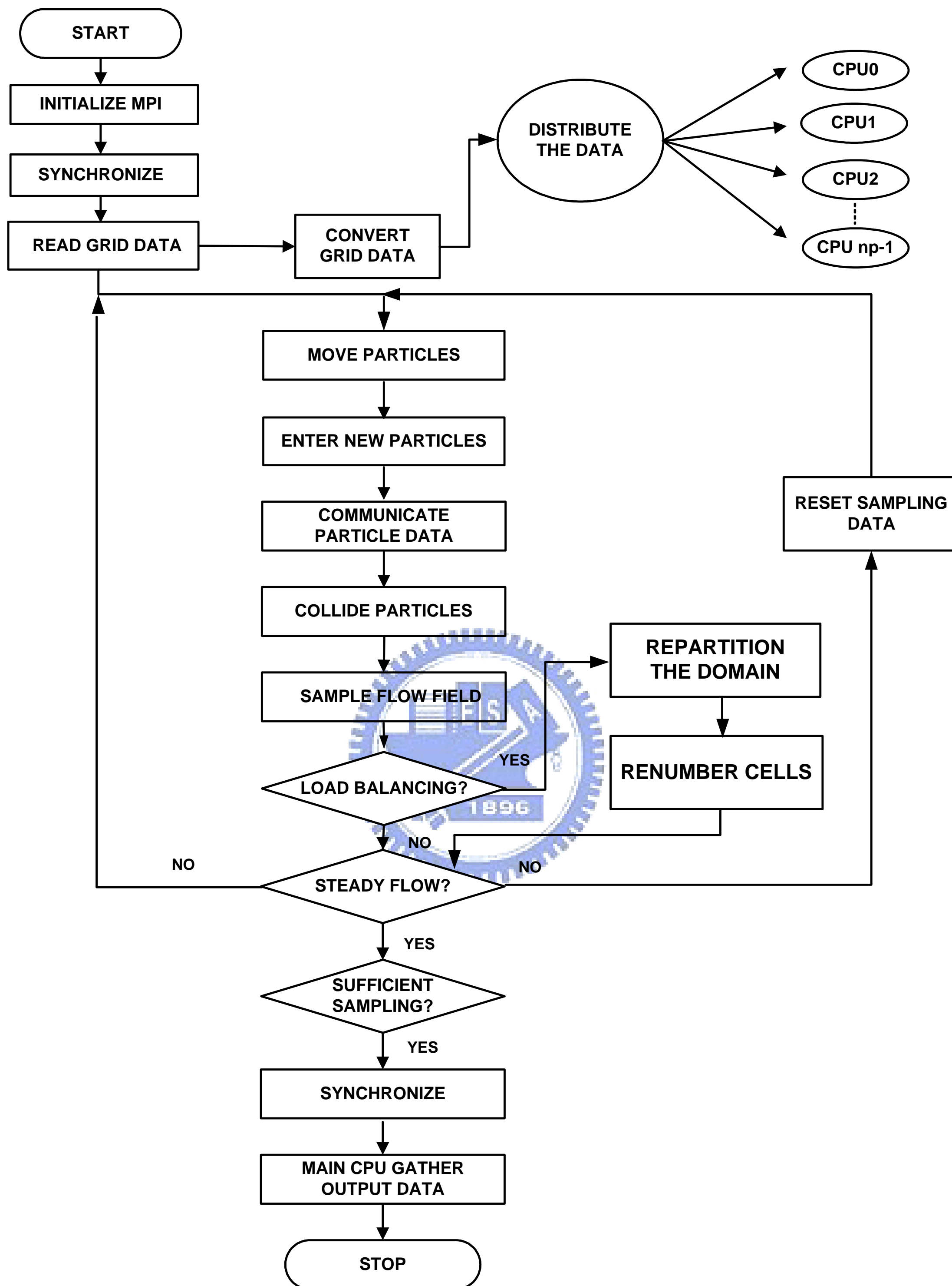


Fig. 2.6 The flowchart of the parallel DSMC method with dynamic domain decomposition method.

Splitting Step

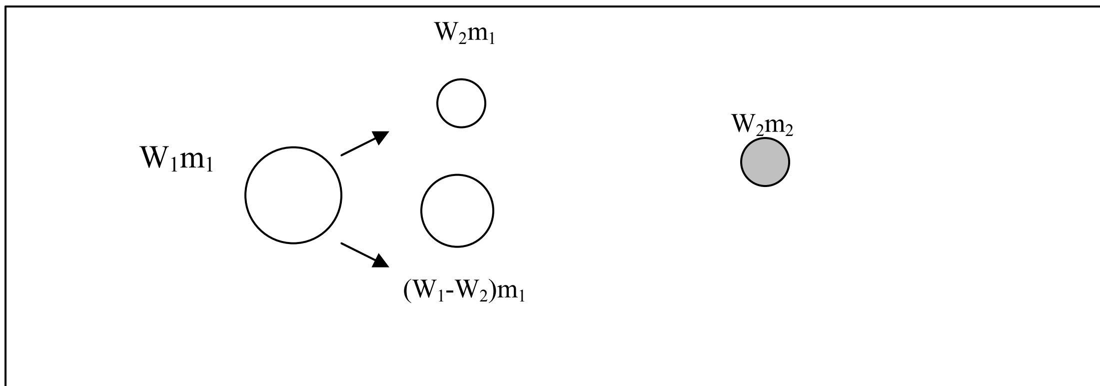


Colliding Step

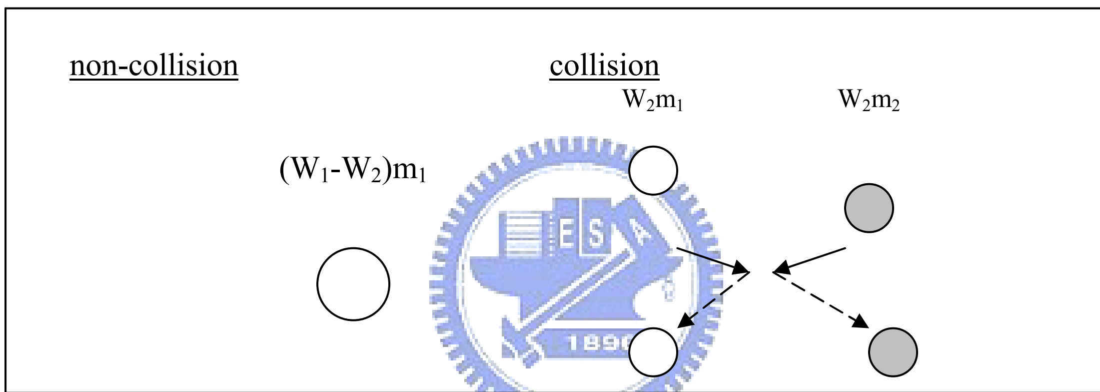


Merging Step

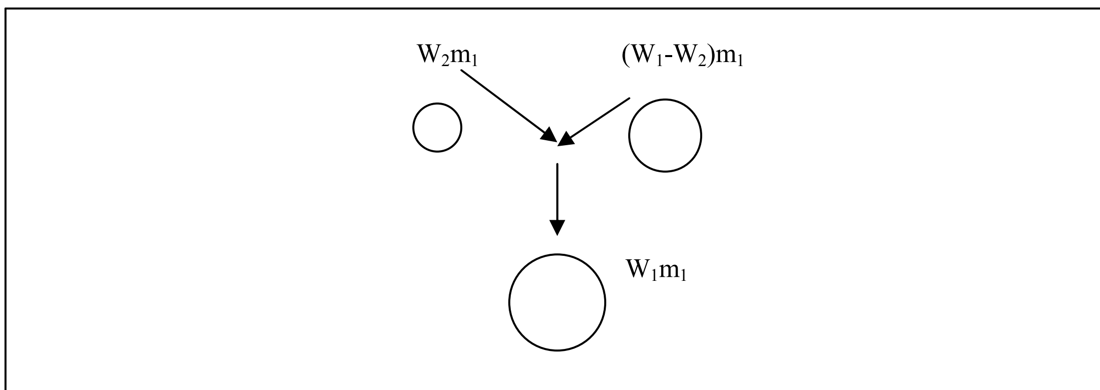


Fig. 2.7 Schematic diagram of CWS for non-reactive flow.

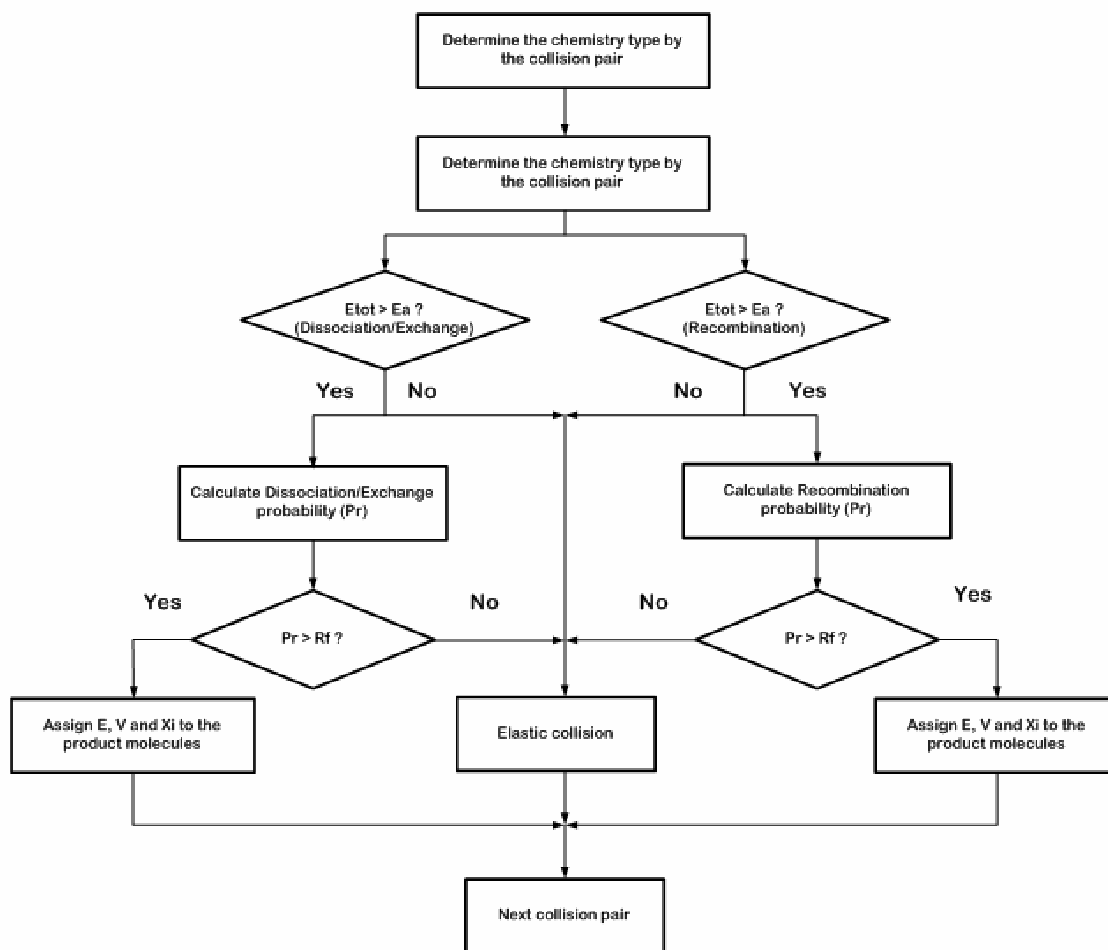


Fig.2.8 The flow chart of chemical reaction in the PDSC.

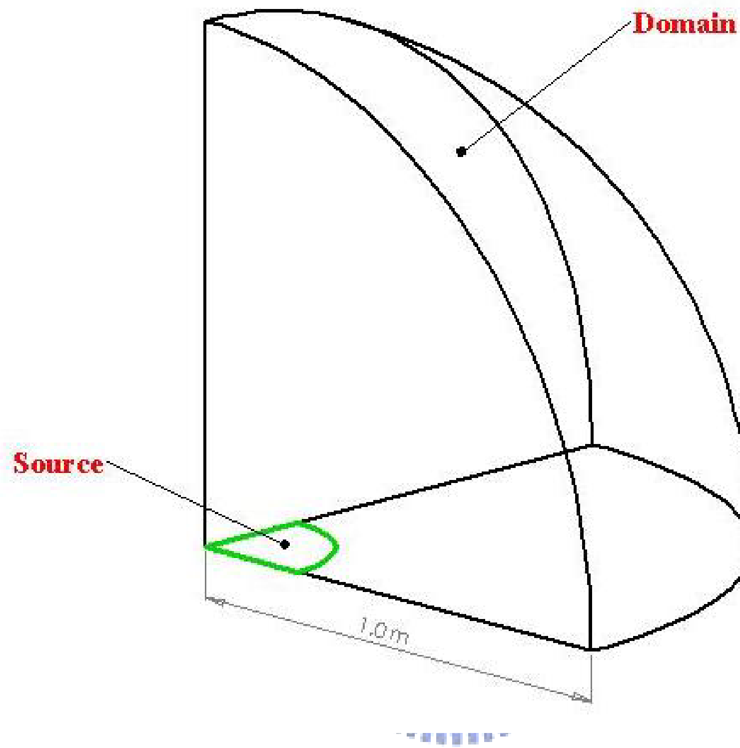


Fig. 3.1 Verification of inflow condition: quarter half sphere for simulation region.

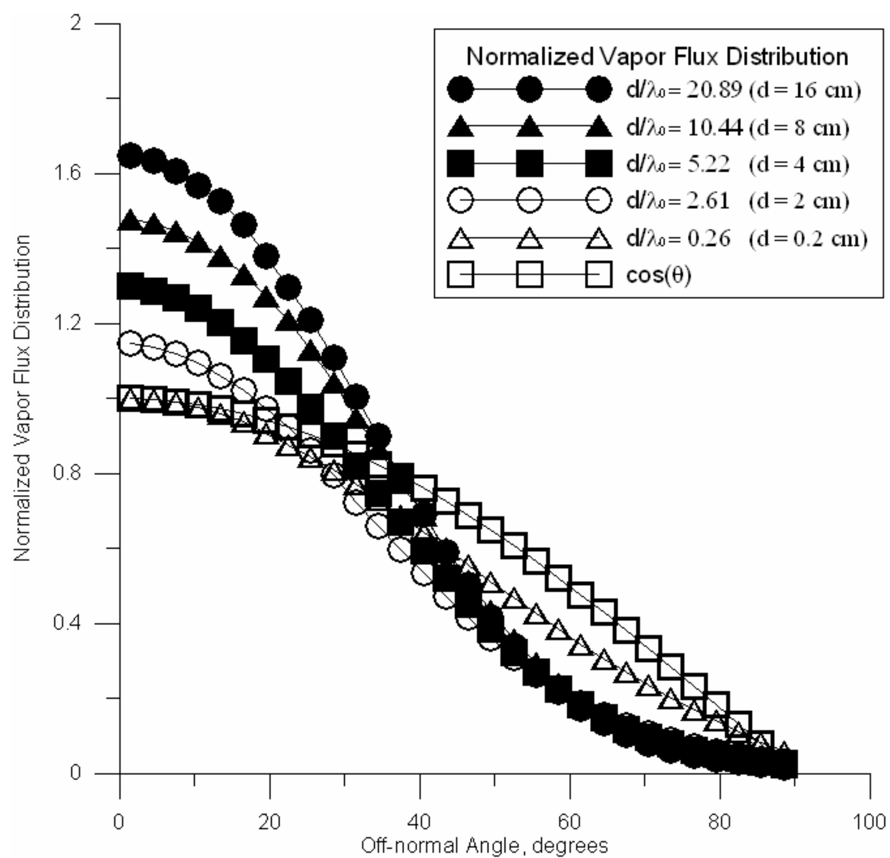


Fig. 3.2 Normalized vapor flux distributions from titanium disk sources at 2050 K with five different diameters, and $\cos(\theta)$ for reference.

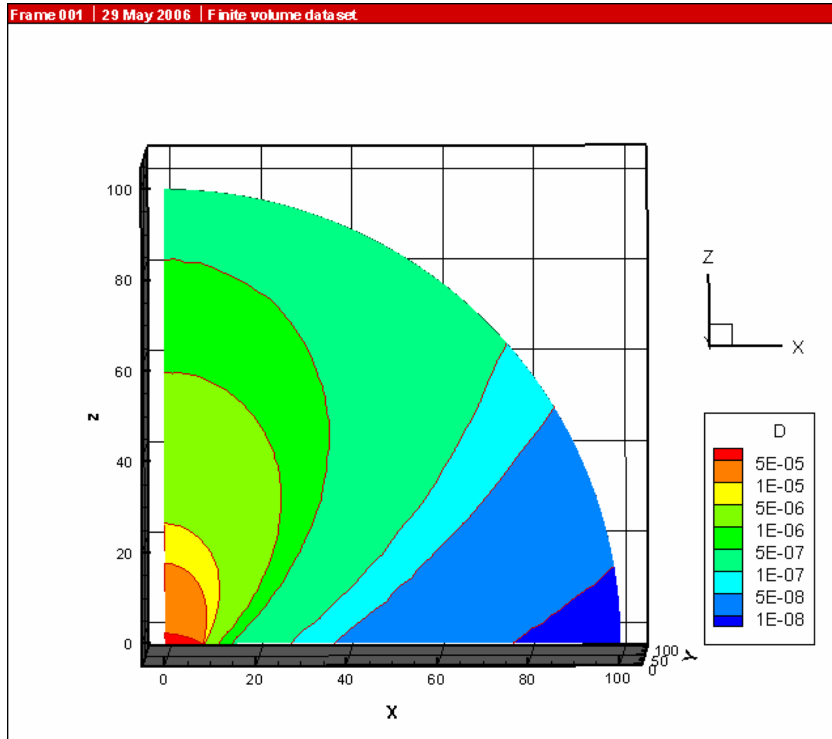


Fig. 3.3 Inflow condition simulation: density distribution.

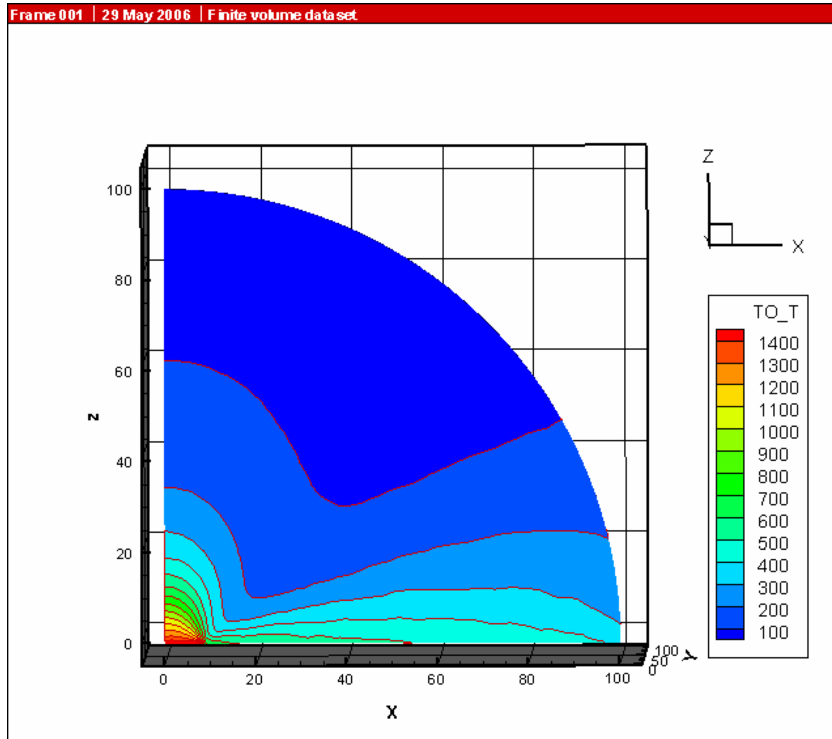


Fig. 3.4 Inflow condition simulation: temperature distribution.

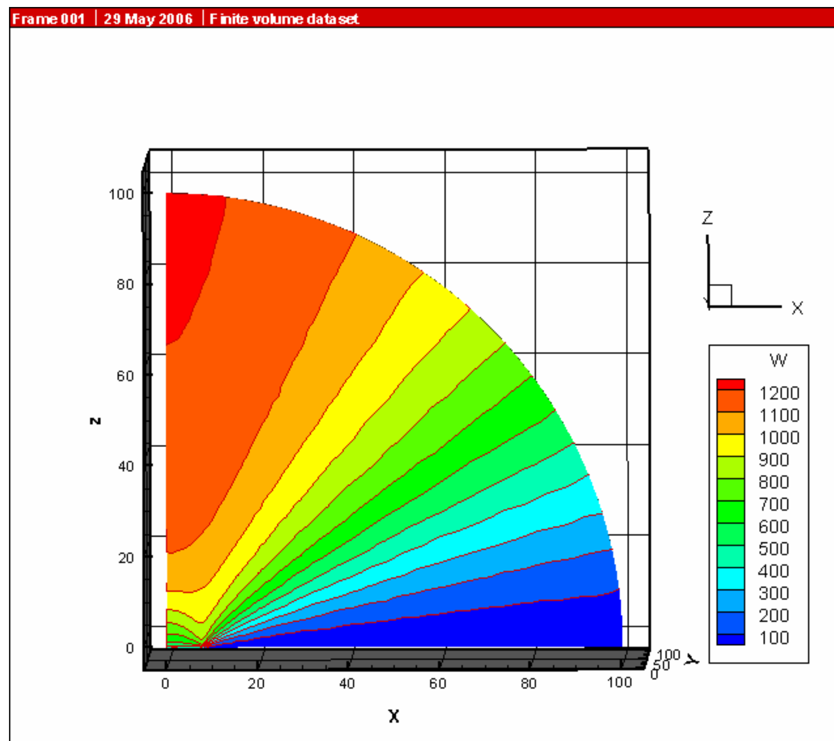


Fig. 3.5 Inflow condition simulation: z-directional velocity distribution.

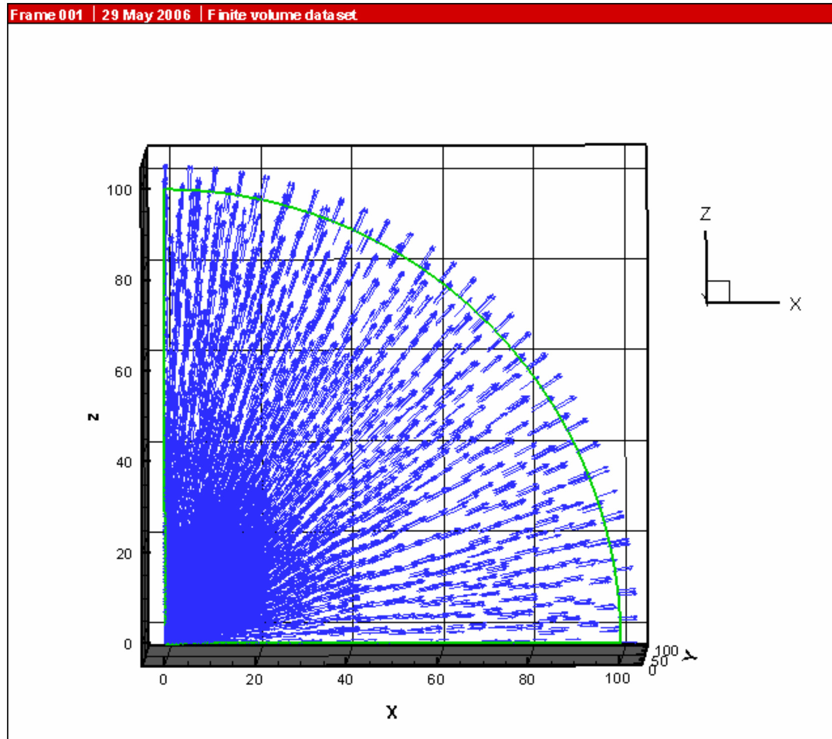


Fig. 3.6 Inflow condition simulation: velocity vector.

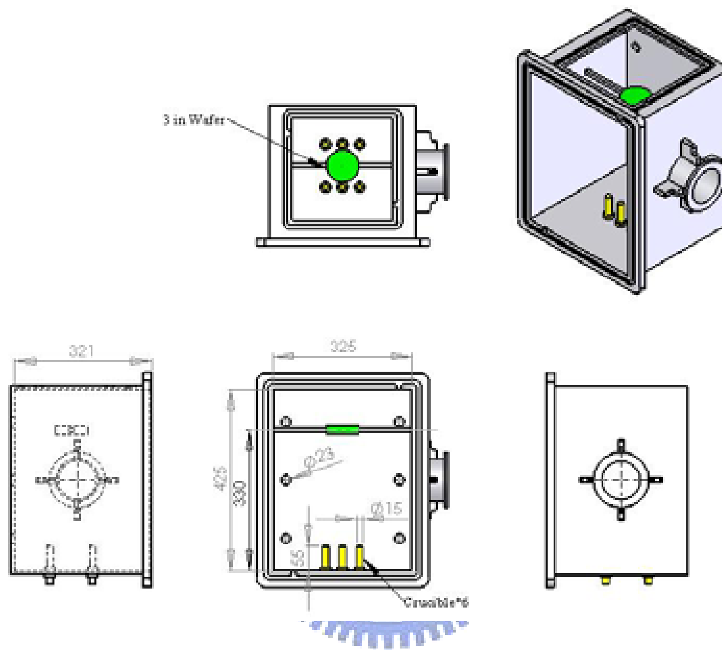


Fig. 3.7 Three view drawing of the chamber.

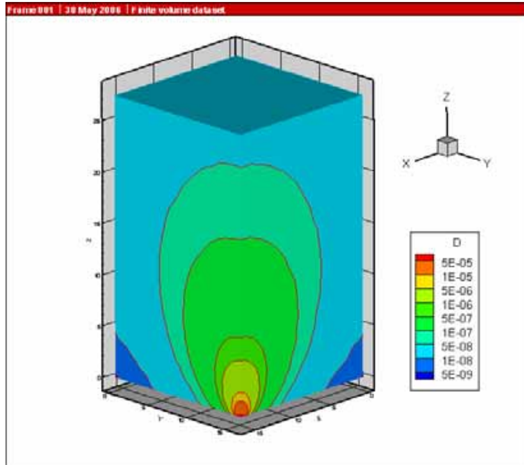


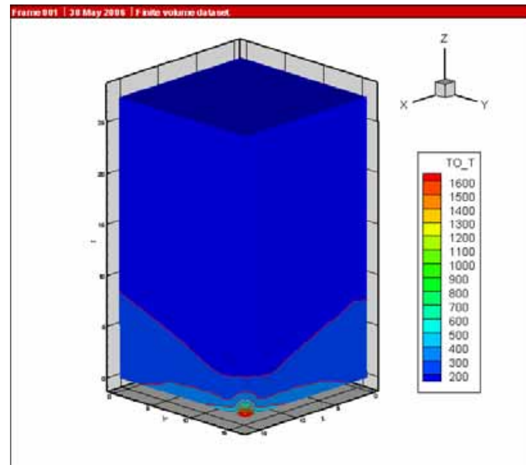


(a) (b)

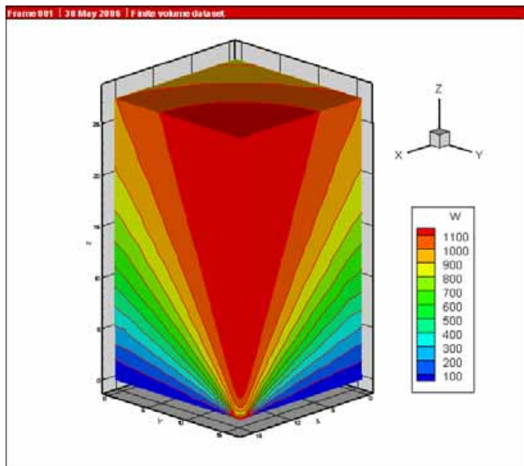


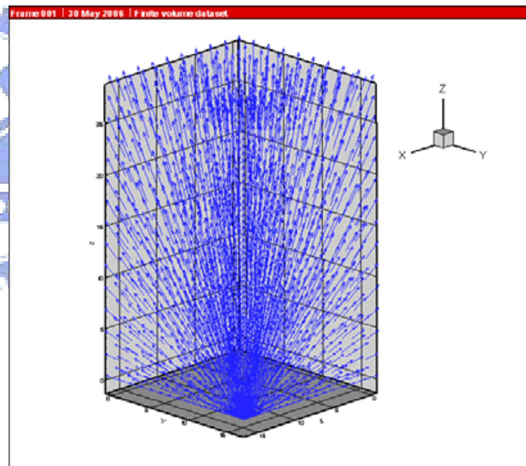


(c) (d)

Fig. 3.8 Inflow condition of quart chamber that contains one source on the bottom: (a) density; (b) temperature; (c) z-directional velocity; (d) velocity vector.

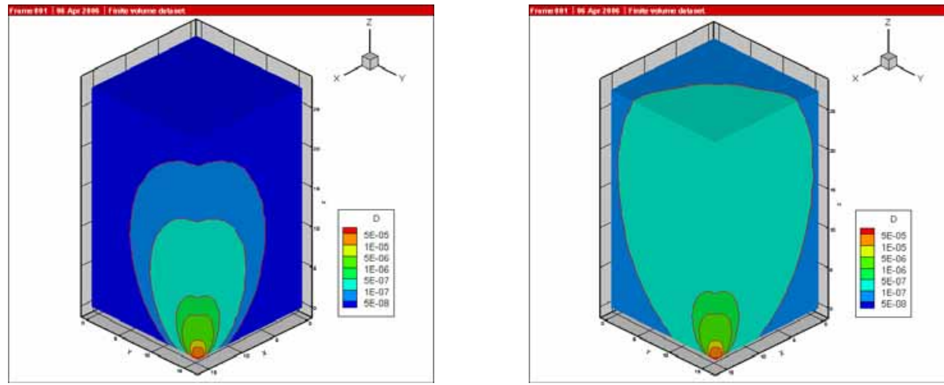


(a)

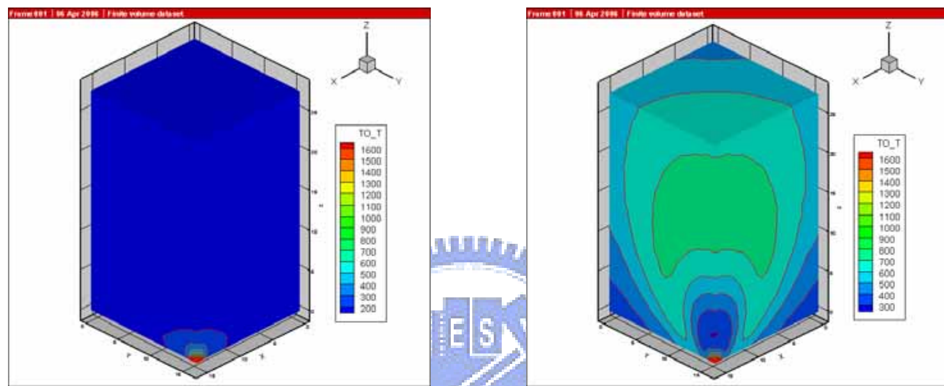


(b)

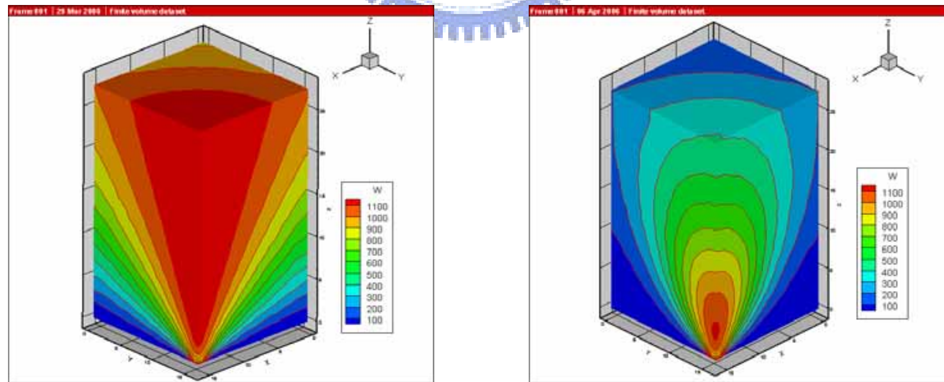


(c)

Fig. 3.9 Comparisons of inflow condition with vacuum (left) and background pressur $5\times10^{-5}$ torr (right): (a) density; (b) temperature; (c) z-directional velocity.

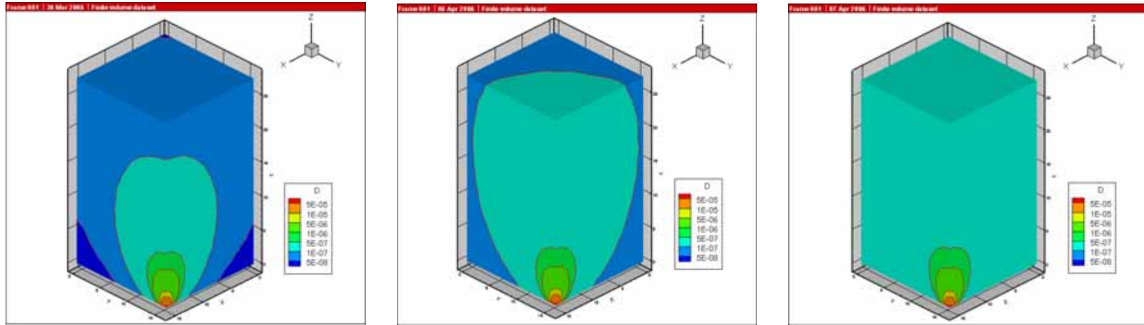


(a)

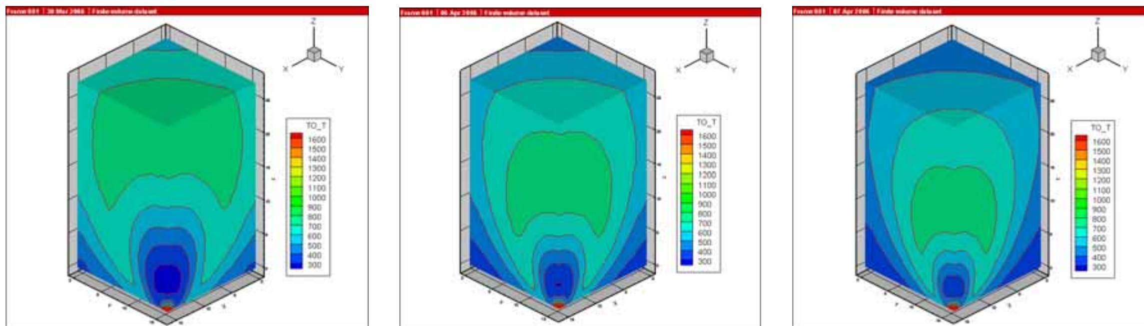


1896

(b)

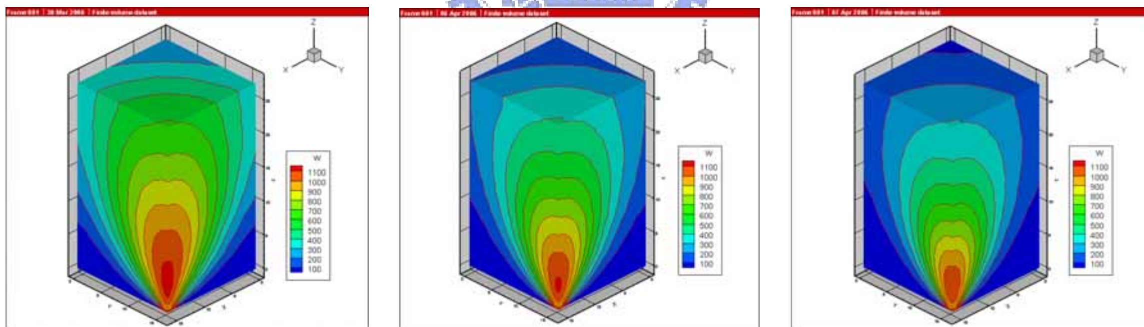


(c)

Fig. 3.10 Comparisons of inflow condition with different background pressure $2.5\times10^{-5}$ torr (left), $5\times10^{-5}$ torr (middle), $7.5\times10^{-5}$ torr (right): (a) density; (b) temperature; (c) z-directional velocity.

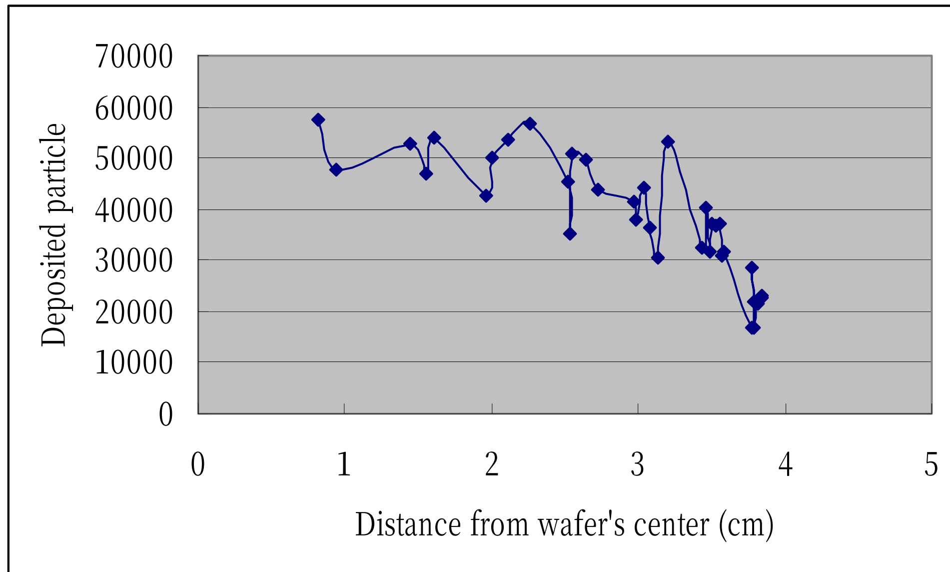


(a)

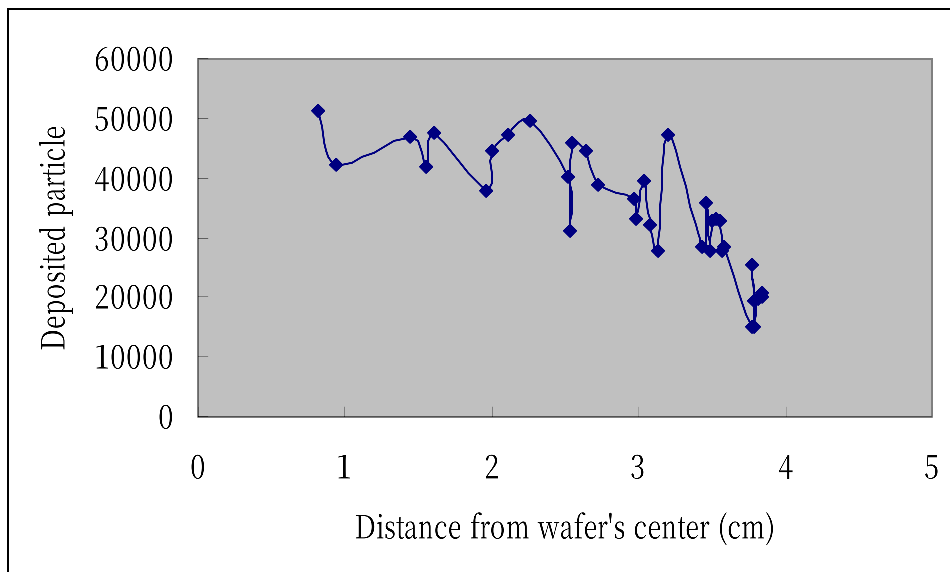


(b)

Fig. 3.11 Comparison of the number deposited particle with (a) vacuum (b) background pressure $7.5\times10^{-5}$ torr.

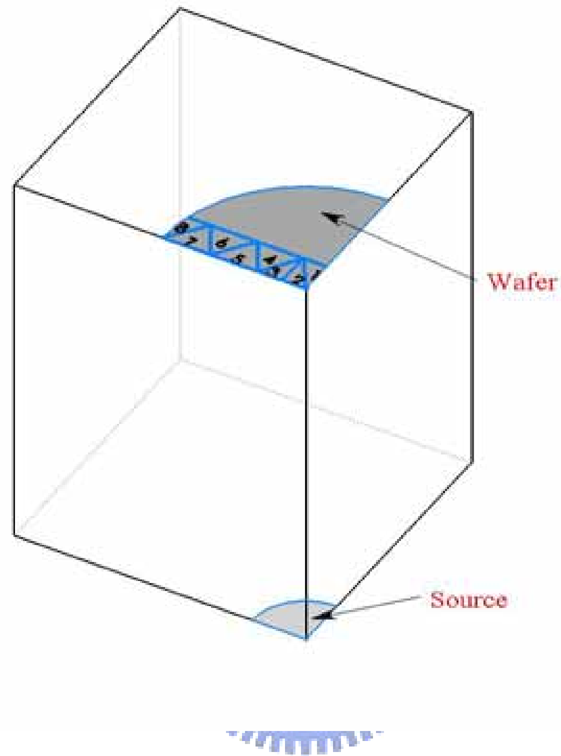


Fig. 3.12 The specific cell labeled to sample the distribution of energy and incident angle.

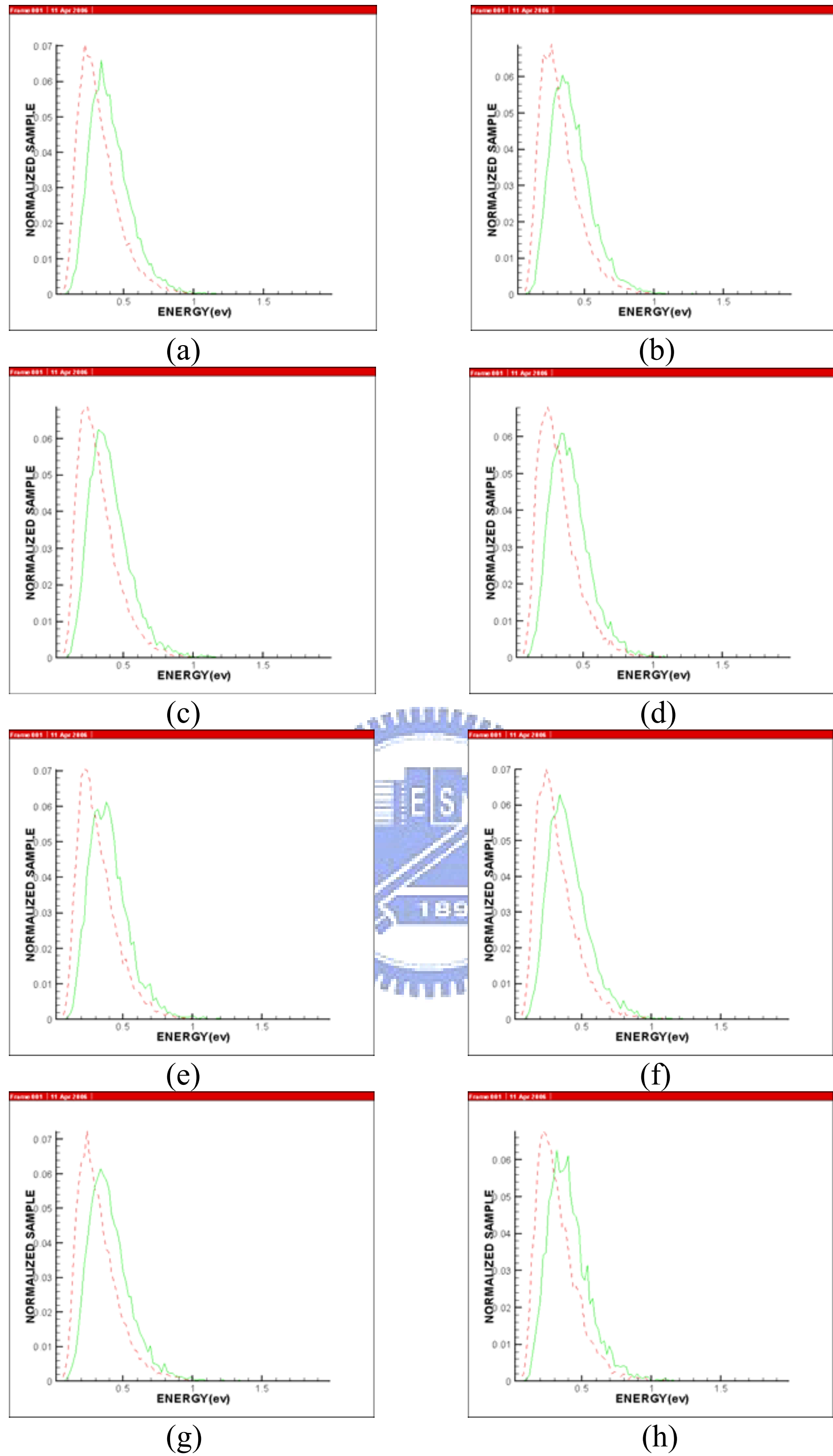


Fig. 3.13 Comparison of energy distribution with vacuum (solid line) and background gas $3.11\times10^{-5}$ torr (dash line): (a) face 1; (b) face 2; (c) face 3; (d) face 4; (e) face 5; (f) face 6; (g) face 7; (h) face 8.

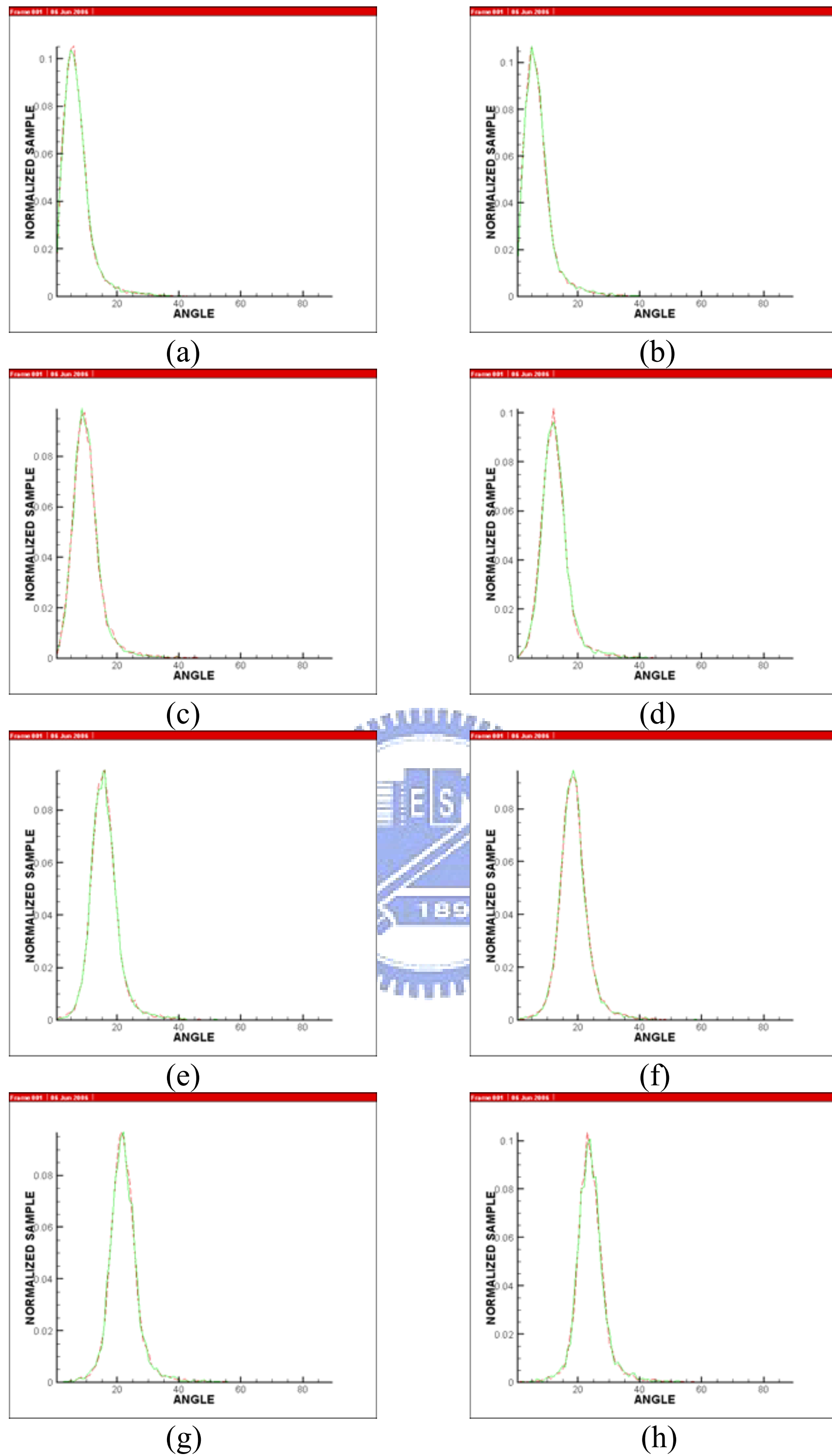


Fig. 3.14 Comparison of incident angle distribution with vacuum (solid line) and background gas $3.11\times10^{-5}$ torr (dash line): (a) face 1; (b) face 2; (c) face 3; (d) face 4; (e) face 5; (f) face 6; (g) face 7; (h) face 8.

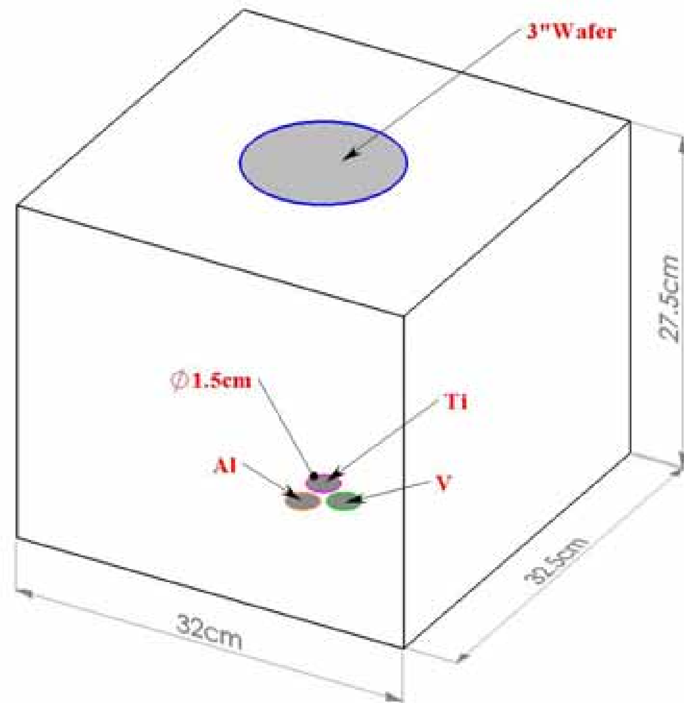


Fig. 3.15 The relative position of three sources and substrate in the simulation domain.

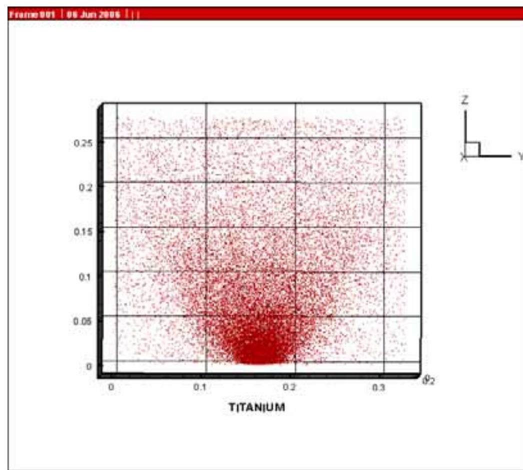


(a)

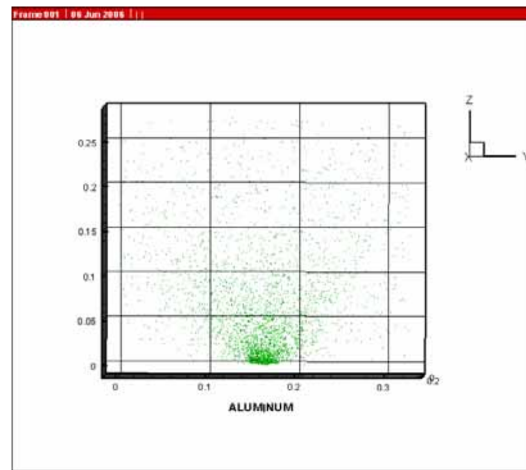


(b)

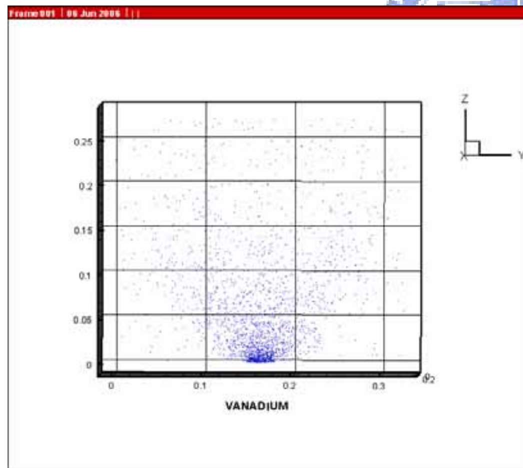


(c)

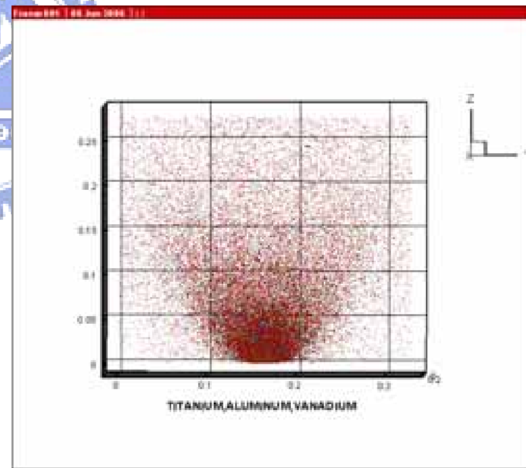


(d)

Fig. 3.16 The position of evaporated atoms at a specific steady time step (a) titanium; (b) aluminum; (c) vanadium; (d) together with titanium, aluminum and vanadium.

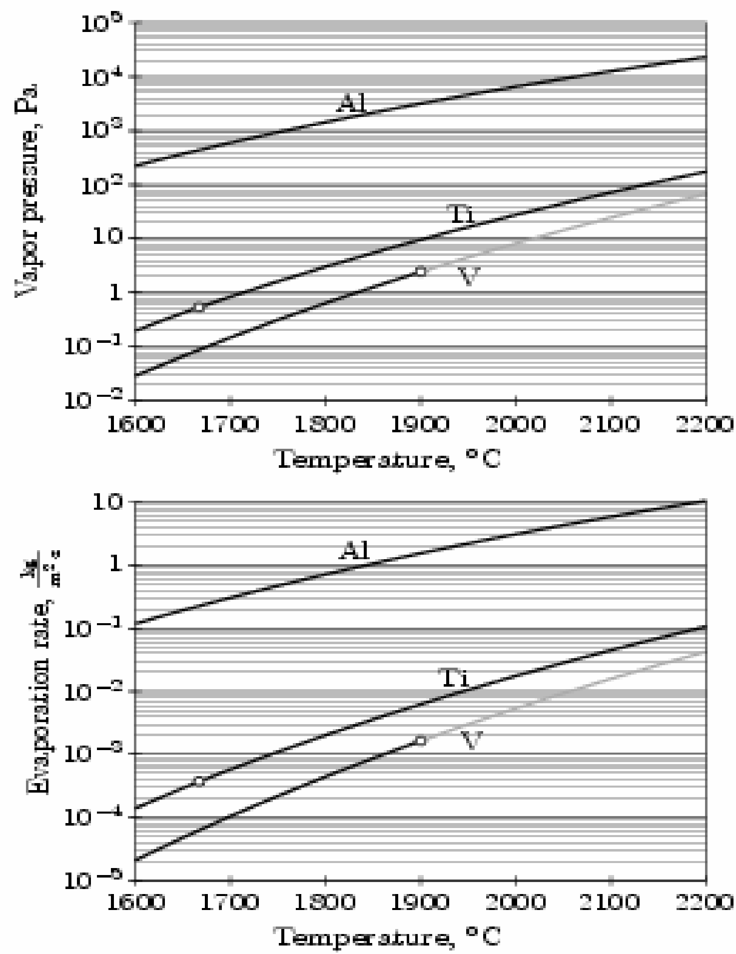


Fig. 3.17 Vapor pressure and Langmuir evaporation rates for titanium, aluminum and vanadium over the range 1600-2200℃. Small circles lie at melting points, and gray vanadium curves are extrapolations of solid data.[Powell, 1997]

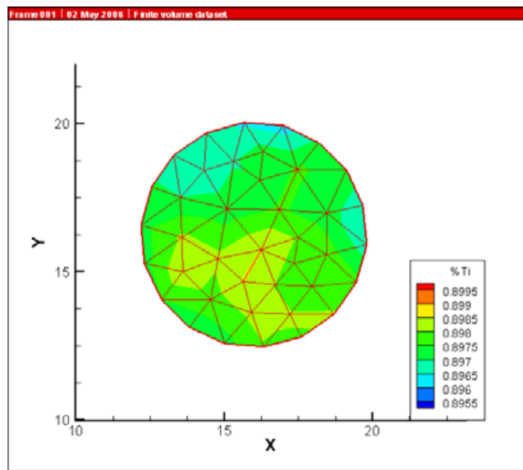


(a)

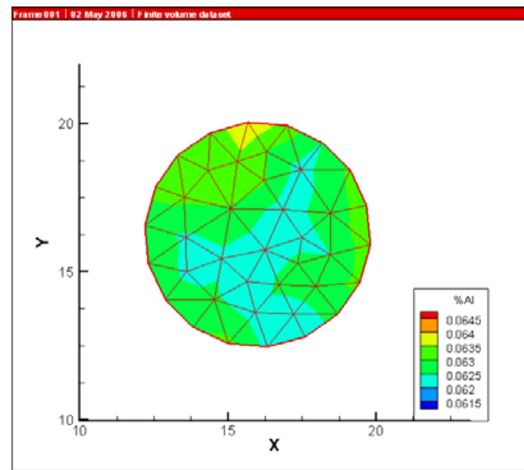


(b)

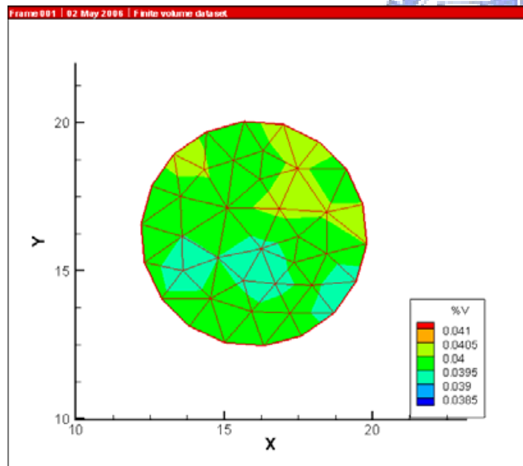


(c)

Fig. 3.18 The distributions of composition of alloy on the substrate (a) titanium; (b) aluminum; (c) vanadium.

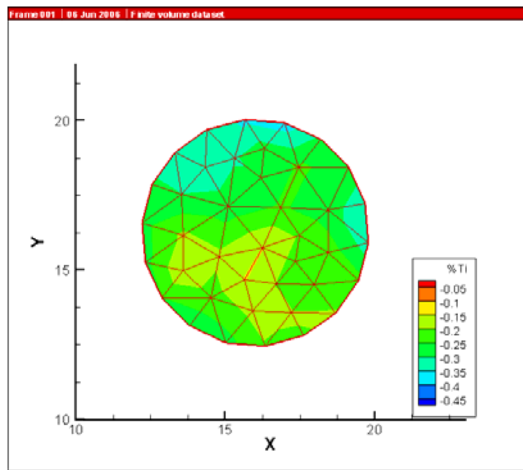


(a)

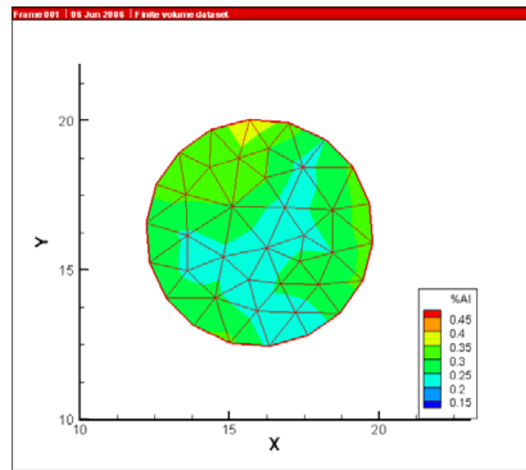


(b)

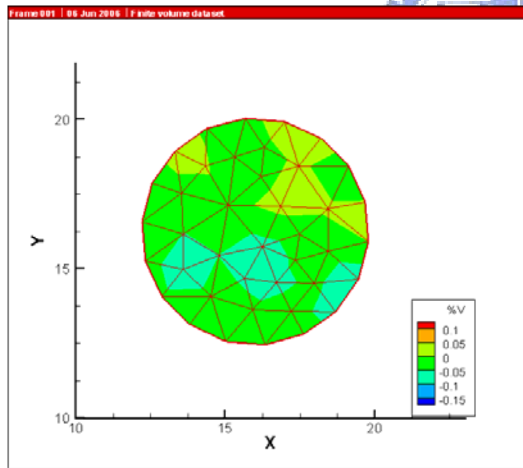


(c)

Fig. 3.19 The distribution of error percentage of individual evaporated atom on the substrate (a) titanium; (b) aluminum; (c) vanadium.

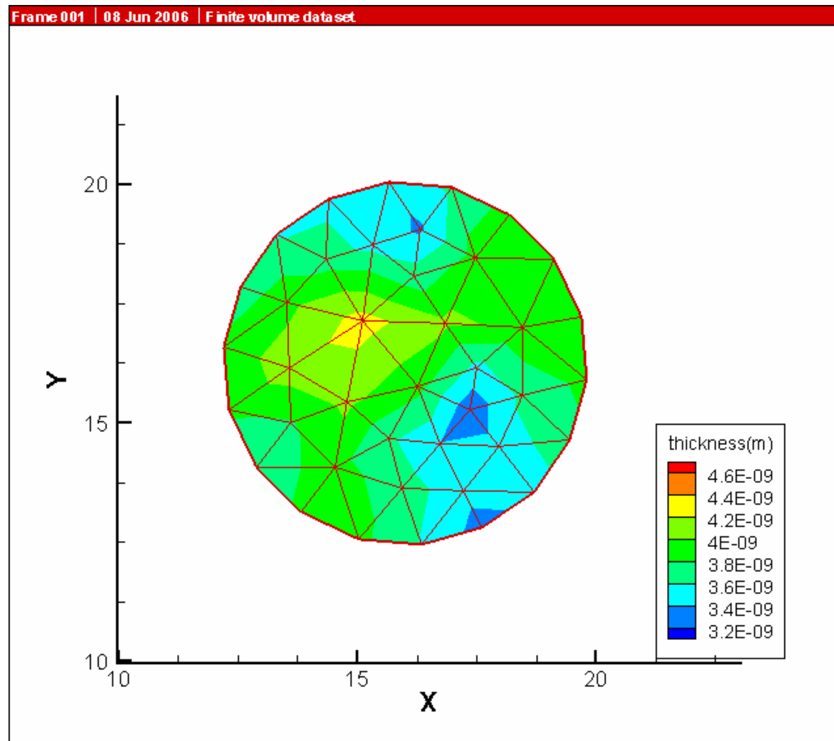


Fig. 3.20 The distribution of thickness on the substrate.

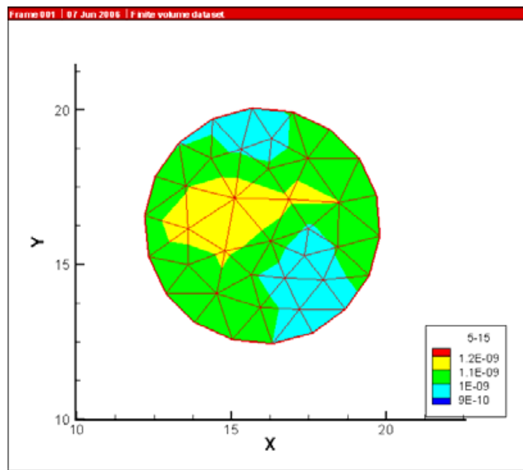


(a)

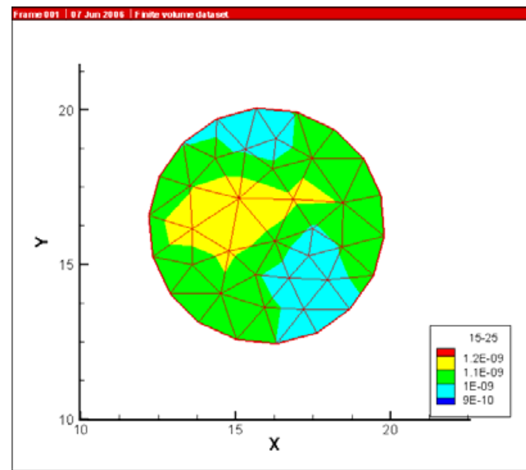


(b)

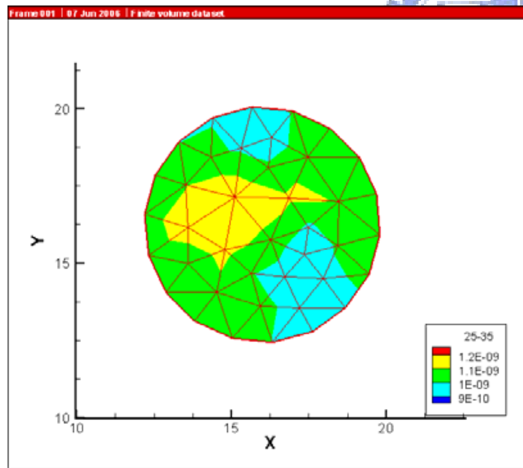


(c)

Fig. 3.21 The distribution of the growth rate at (a) time step 5000~15000; (b) time step 15000~25000; (c) time step 25000~35000.

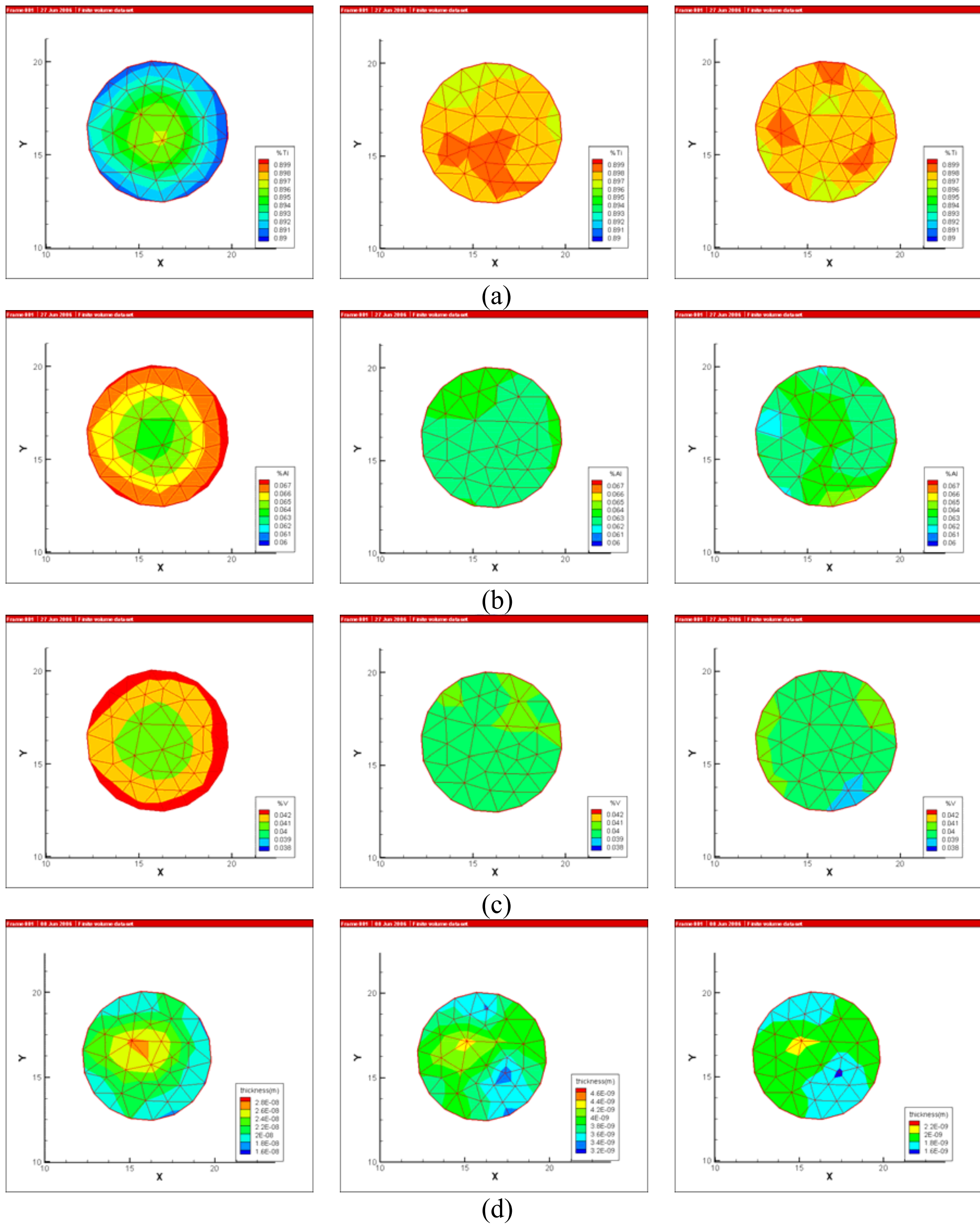


Fig. 3.22 The comparisons of composition and thickness. The rows of left, middle and right represent three different altitude of the substrate: 10cm, 27.5cm and 40cm. The columns represent (a) titanium; (b) aluminum; (c) vanadium; (d) thickness.

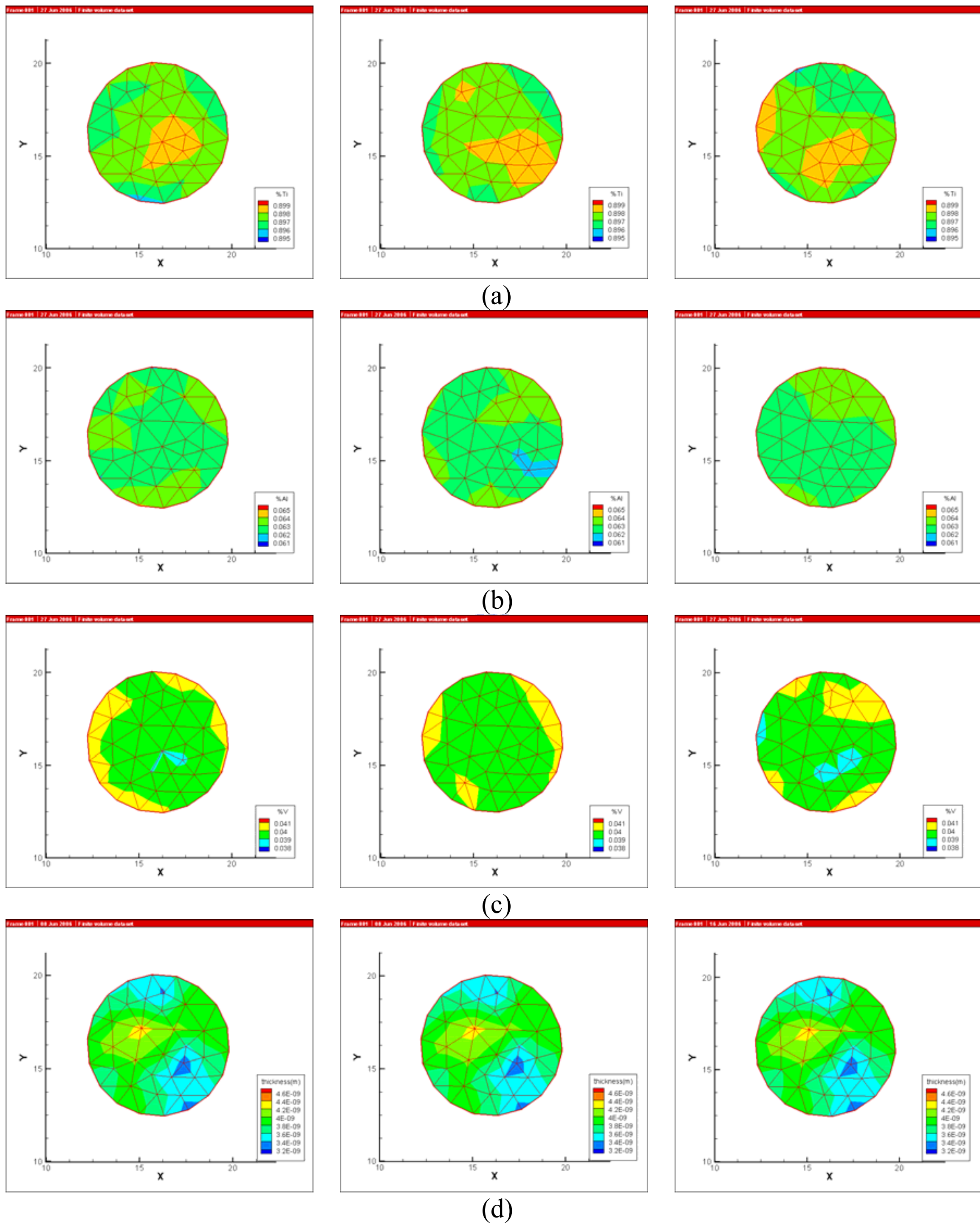


Fig. 3.23 The comparisons of composition and thickness. The rows of left, middle and right represent three different background pressure: $5\times10^{-5}$, $5\times10^{-6}$ torr and vacuum. The columns represent (a) titanium; (b) aluminum; (c) vanadium; (d) thickness.

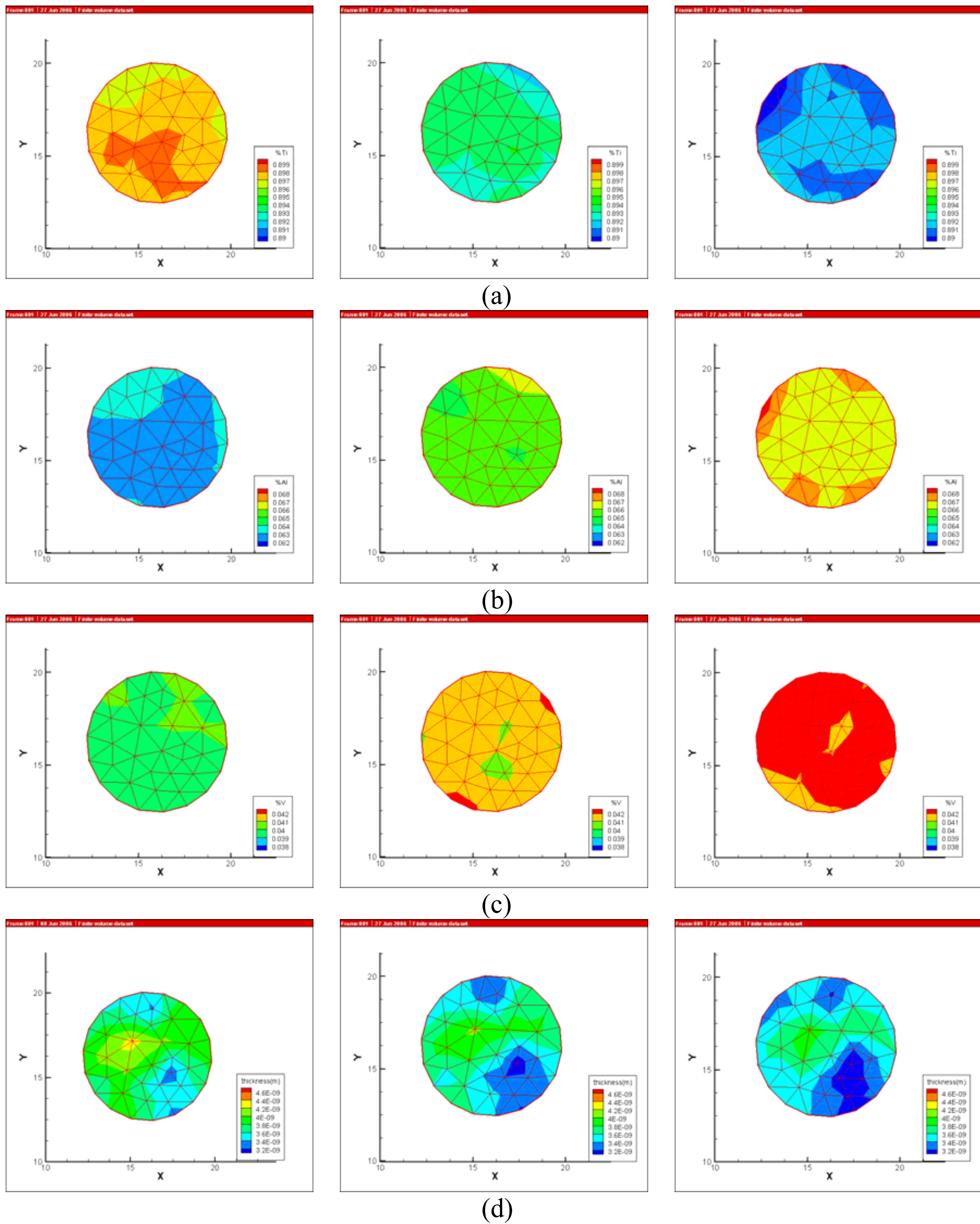


Fig. 3.24 The comparisons of composition and thickness. The rows of left, middle and right represent three different distances between sources: 1.732, 4.330 and 6.928cm. The columns represent (a) titanium; (b) aluminum; (c) vanadium; (d) thickness.